ACCEPTED BY THE ASTROPHYSICAL JOURNAL 2013 DECEMBER 26; PUBLISHED 2014 FEBRUARY 12
Preprint typeset using LaTeX style emulateapj v. 04/17/13

arXiv:1401.5074v2 [astro-ph.CO] 13 Feb 2014

# STATISTICAL PROPERTIES OF MULTI-EPOCH SPECTRAL VARIABILITY OF SDSS STRIPE 82 QUASARS

MITSURU KOKUBO[1], TOMOKI MOROKUMA[1], TAKEO MINEZAKI[1], MAMORU DOI[1,2,3],
TOSHIHIRO KAWAGUCHI[4], HIROAKI SAMESHIMA[5], AND SHINTARO KOSHIDA[6]
[1] Institute of Astronomy, School of Science, the University of Tokyo, 2-21-1 Osawa, Mitaka,Tokyo 181-0015, Japan; mkokubo@ioa.s.u-tokyo.ac.jp
[2] Kavli Institute for the Physics and Mathematics of the Universe (WPI), Todai Institutes for Advanced Study,
The University of Tokyo, 5-1-5 Kashiwanoha, Kashiwa, Chiba 277-8583, Japan
[3] Research Center for the Early Universe, the University of Tokyo, 7-3-1 Hongo, Bunkyo-ku, Tokyo 113-0033, Japan
[4] Department of Physics and Information Science, Yamaguchi University, Yamaguchi, Yamaguchi 753-8512, Japan
[5] Institute of Space and Astronautical Science, Japan Aerospace Exploration Agency, 3-1-1 Yoshinodai, Sagamihara, Kanagawa 252-5210, Japan
[6] Center of Astro Engineering and Department of Electrical Engineering, Pontificia Universidad Catolica de Chile, Av. Vicuña Mackenna 4860, Santiago, Chile
*Accepted by the Astrophysical Journal 2013 December 26; Published 2014 February 12*

## ABSTRACT

We investigate the UV−optical (longward of Ly$\alpha$ 1216Å) spectral variability of nearly 9000 quasars ($0 < z < 4$) using multi-epoch photometric data within the SDSS Stripe 82 region. The regression slope in the flux−flux space of a quasar light curve directly measures the color of the flux difference spectrum, then the spectral shape of the flux difference spectra can be derived by taking a careful look at the redshift dependence of the regression slopes. First, we confirm that the observed quasar spectrum becomes bluer when the quasar becomes brighter. We infer the spectral index of the composite difference spectrum as $\alpha_\nu^{\rm dif} \sim +1/3$ (in the form of $f_\nu \propto \nu^{\alpha_\nu}$), which is significantly bluer than that of the composite spectrum $\alpha_\nu^{\rm com} \sim -0.5$. We also show that the continuum variability cannot be explained by the accretion disk models with varying mass accretion rate. Second, we examine the effects of broad emission line variability on the color-redshift space. The variability of the "Small Blue Bump" is extensively discussed. We show that the low-ionization lines of Mg II and Fe II are less variable compared to Balmer emission lines and high-ionization lines, and the Balmer continuum is the dominant variable source around $\sim$ 3000Å. These results are compared with previous studies, and the physical mechanisms of the variability of the continuum and emission lines are discussed.

*Subject headings:* accretion, accretion disks − galaxies: active − galaxies: nuclei − quasars: emission lines − quasars: general

## 1. INTRODUCTION

The flux variability of quasars, or active galactic nuclei (AGNs), have been observed on timescales ranging from hours to decades. UV−optical emissions are thought to arise from an accretion disk surrounding a central supermassive black hole. UV−optical variability has been considered a powerful tool for examining the nature of AGN central engine (Vanden Berk et al. 2004; Kouzuma & Yamaoka 2012, and references therein).

Spectral variability (i.e., wavelength dependence of the flux variation) provides important clues for underlying physics. One of the well-known features of AGN UV−optical variability is that the color tends to become bluer when it gets brighter (e.g., Maoz et al. 1993; Paltani & Courvoisier 1994; Giveon et al. 1999; Vanden Berk et al. 2004; Sakata et al. 2011; Schmidt et al. 2012; Zuo et al. 2012), which is used to constrain the accretion disk models in several previous works (e.g., Schmidt et al. 2012, and references therein). This bluer-when-brighter trend is also important for studies of the emission line formation, as a change of the spectral energy distribution of the ionizing continuum has significant effects on the physical state of the emission line region (e.g., Korista & Goad 2004). However, as noted in Sakata et al. (2010), the "observed" bluer-when-brighter trend admits a dual interpretation: (1) the variable component, which is probably the accretion disk emission itself, becomes brighter and gets bluer (e.g., Wamsteker et al. 1990; Giveon et al. 1999; Webb & Malkan 2000; Vanden Berk et al. 2004; Wilhite et al. 2005), and (2) the variable component of constant color becomes brighter and increasingly dominant over the non-variable components of red color, which is mainly composed of host galaxy flux (e.g., Choloniewski 1981; Winkler et al. 1992; Winkler 1997; Paltani & Walter 1996; Suganuma et al. 2006). That is, the "observed" bluer-when-brighter trend does not directly imply AGN intrinsic spectral hardening. Moreover, we have to be careful of the effect of the broad emission lines (BELs) when analyzing the broad-band photometric variability, because they have large amount of flux and are variable themselves. Sakata et al. (2010) investigated the color variability of 11 nearby Seyfert galaxies, estimating the effect of non-variable components, and concluded that interpretation (2) is valid for the AGN intrinsic continuum emission in the optical region, which kept the constant spectral shape during the flux variation. The same result was obtained by Woo et al. (2007) and Walsh et al. (2009). On the other hand, Sakata et al. (2011) did the same kind of analyses as Sakata et al. (2010) for 10 Sloan Digital Sky Survey (SDSS) high redshift quasars and concluded that AGN intrinsic spectra actually became steeper as it got brighter in the UV region, which indicates that interpretation (1) is valid in the UV region. Wilhite et al. (2005) used two-epoch spectral data for $\sim$ 300 SDSS quasars and concluded that the composite flux difference spectrum is steeper than the composite spectrum in the UV range but it has the same spectral index in the optical range. Note that the effects of the contamination from non-variable components, which are undoubtedly existing at least in part in the composite spectrum (e.g., Glikman et al. 2006; Vanden Berk et al. 2006) are not evaluated in Wilhite et al. (2005). Thus, a consensus about the properties of the color variability of AGNs

has not been obtained yet (see e.g., Bian et al. 2012; Zhang 2013).

The difficulties of variability studies have led to the uncertainties of the AGN variability model. A number of models have been developed attempting to explain AGN variability such as X-ray reprocessing (Krolik et al. 1991), instabilities in the accretion disk (Kawaguchi et al. 1998; Dexter & Agol 2011), gravitational microlensing (Hawkins 1993), star collisions (Torricelli-Ciamponi et al. 2000), and multiple supernovae or starbursts near the nucleus (Terlevich et al. 1992). Recently, several authors have claimed that the AGN variability is due to the changes in accretion rate (Pereyra et al. 2006; Li & Cao 2008; Sakata et al. 2011; Zuo et al. 2012; Gu & Li 2013), which seems to explain the larger variability in the shorter wavelengths quantitatively. Sakata et al. (2011) fitted the standard accretion disk model (Shakura & Sunyaev 1973) with a varying accretion rate for the light curves of 10 SDSS quasars and concluded that this model could correctly explain the color variability. Gu & Li (2013) also obtained the same conclusion for eighteen steep spectrum radio quasars. However, Schmidt et al. (2012) investigated the color variability of $\sim 9000$ SDSS Stripe 82 quasars and concluded that the color variability of quasars cannot be described by the several accretion disk models (Davis et al. 2007) with varying accretion rate, as the color of quasars becomes bluer than the model predictions. Trèvese & Vagnetti (2002) also pointed out that the changes of accretion rate are insufficient to explain the amount of spectral variation.

In the present work, we focus on the model of Pereyra et al. (2006), which assumes that the AGN variability is caused by small changes in the mass accretion rate in the standard thermal accretion disk (Shakura & Sunyaev 1973) and predict the flux difference spectrum between one epoch to another. We note that although we cannot directly observe the intrinsic AGN spectra or intrinsic color, we can directly observe the color of the variable portion in AGN spectra (i.e., the flux difference spectrum). This can be achieved by using the "flux−flux correlation method" described in Section 3, which relies on the fact that UV−optical, two-band flux to flux plots of AGN broad-band light curves show strong linear correlation (e.g., Choloniewski 1981; Sakata et al. 2011; Lira et al. 2011, and references therein). As mentioned earlier, the flux variability occurs not only in the continuum emission, but also in the BELs. In general, the quasar variability (obtained by broad-band photometry) is dominated by continuum variability (intrinsic Baldwin effect, e.g., Wilhite et al. 2005; Shields 2007), but we are probably able to see some amount of variable emission line components in it. We can also examine the effects of the BEL variability on the broad band photometry by taking a careful look at our result, which has not been well studied in previous works.

In this paper, we investigate the years-time-scale UV−optical spectral variability of large quasar samples in SDSS Stripe 82 region, attempting to derive some insight to the physical mechanisms of AGN variability. Our standpoint is summarized as below:

- Using the flux−flux correlation method, we derive the color of the flux difference spectrum for each quasar and for each band pair model-independently. Then, we investigate the rest-frame wavelength dependence of the quasar spectral variability by taking a careful look at the redshift dependence of the color of the flux difference spectrum, with the assumption that there is no redshift-dependence in the rest-frame spectral variability (e.g., Schmidt et al. 2012; Zuo et al. 2012). The derived flux difference spectrum can be directly compared with the AGN UV−optical variability model presented in Pereyra et al. (2006).

- We do not assume any models or estimates of non-variable components such as host galaxy flux or narrow line emissions in the present work. This means that the color variability trend (bluer-when-brighter or achromatic variation) referred to in this paper is actually the "observed" color variability trend, not the AGN intrinsic variation in spectral shape. However, as shown by Sakata et al. (2011) (see also Croom et al. 2009; Krawczyk et al. 2013), host galaxy flux and narrow emission lines in SDSS bandpasses are probably negligible for intermediate and high redshift quasars. Thus the "observed" color variability trend, particularly in rest-frame UV wavelengths, can be considered as the intrinsic variation in AGN continuum spectral shape, although the effects of the variability of BELs should be taken into consideration.

In Section 2 we describe a database of SDSS Stripe 82 multi-epoch five-band light curves from the SDSS data, and we introduce the flux−flux correlation method (Choloniewski 1981) in Section 3. In Section 4, we show the linear regression slopes in flux−flux space for quasar light curves, which correspond to the color of the flux difference spectrum, as a function of redshift. Then, we compare our results with previous works and the standard thin-disk model. We discussed the emission line variability in Section 5. The variability of the Small Blue Bump (SBB) spectral region is discussed separately in Section 6. Finally, we summarize our conclusions in Section 7. The adopted models for emission lines and intergalactic medium (IGM) attenuation used in Section 5 are described in Appendix A, and the results of the regression intercept, which are not concerned with the main results in this paper, are interpreted and shown in Appendix B.

## 2. DATA

We use a database of SDSS Stripe 82 multi-epoch five-band light curves for spectroscopically confirmed quasars presented by MacLeod et al. (2012). Their Southern sample catalog contains recalibrated $\sim$10 yr light curves for 9258 quasars in the SDSS Data Release 7 (DR7; Abazajian et al. 2009). SDSS magnitude is converted to flux unit. The SDSS system is nearly the AB system (zero-point flux density = 3631 Jy), but the photometric zero-points are slightly off the AB standard. We apply the correction for the zero-point offset between the SDSS system and the AB system following the recommendations in the SDSS instructions[1]: $u_{\rm AB} = u_{\rm SDSS} - 0.04$, $g_{\rm AB} = g_{\rm SDSS}$, $r_{\rm AB} = r_{\rm SDSS}$, $i_{\rm AB} = i_{\rm SDSS}$ and $z_{\rm AB} = z_{\rm SDSS} + 0.02$ . In this paper, "Flux" means $f_\nu$ unit (i.e., Jansky unit), but we also use $f_\lambda$ unit when we refer to the spectral shape. These two are related as $f_\nu = \lambda^2 f_\lambda / c$, and power-law indices are related as $\alpha_\nu = -2 - \alpha_\lambda$, where $f_\nu \propto \nu^{\alpha_\nu}$ and $f_\lambda \propto \lambda^{\alpha_\lambda}$.

We cross-match the Southern sample light curve catalog with a catalog of quasar properties from SDSS DR7 (Shen et al. 2011)(the maximum search radius is 2 arcsec). We use the improved redshift from Hewett & Wild (2010) as the redshift of each quasar. In the present paper, we use a

[1] http://www.sdss.org/dr7/algorithms/fluxcal.html

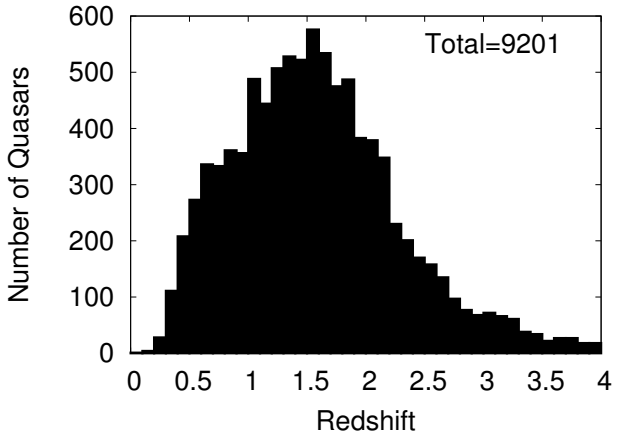


FIG. 1.— Redshift distribution ($0 < z < 4$) of the SDSS Stripe 82 quasar sample.

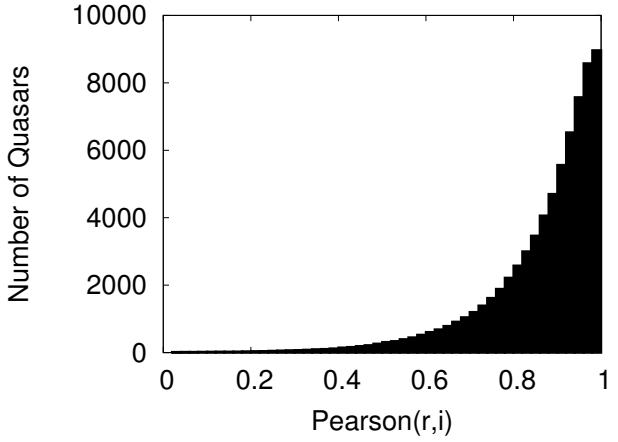


FIG. 2.— Cumulative distribution of Pearson correlation coefficient in flux−flux space (*x*-axis = *r*-band flux, and *y*-axis = *i*-band flux) for light curves of our sample ($0 < z < 4$) observed more than 20 epochs (see Section 3.5 for more details of our sample).

sample of quasars within the redshift range from 0 to 4, in which there are 9201 quasars. The redshift distribution of the sample ($0 < z < 4$) is shown in Figure 1.

Galactic absorption is corrected using $A_u$[mag] tabulated in the database of MacLeod et al. (2012) for each quasar, where $A_g$, $A_r$, $A_i$, $A_z$ = 0.736, 0.534, 0.405, 0.287 $\times$ $A_u$ (Schlegel et al. 1998; MacLeod et al. 2012).

## 3. THE FLUX-FLUX CORRELATION METHOD

In this section, we introduce the flux−flux correlation method and discuss the advantages of the use of this method.

### 3.1. *The Color of the Flux Difference Spectrum in Flux-Flux Space*

We introduce flux−flux correlation method (Choloniewski 1981; Winkler et al. 1992; Lyutyi & Doroshenko 1993; Hagen-Thorn 1997) as an alternative to magnitude−magnitude or magnitude−color correlation analyses. Choloniewski (1981) first noticed that the quasars' UV−optical fluxes have a linear correlation in flux−flux space, and several authors have since confirmed it (e.g., Winkler 1997; Glass 2004; Sakata et al. 2011; Lira et al. 2011; Gu & Li 2013). In Figure 2, we show the Pearson

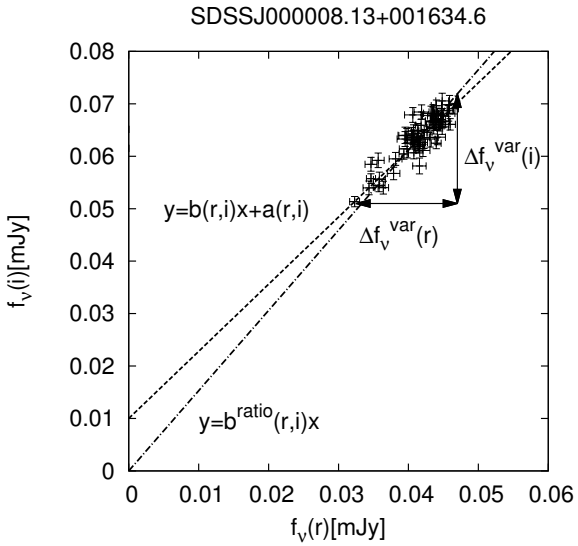


FIG. 3.— Illustration for the flux−flux correlation method. The linear regression line is $y = 1.28x + 0.01$ [mJy] (i.e., $b(r,i) = \Delta f_\nu^{\rm var}(i)/\Delta f_\nu^{\rm var}(r) = 1.28$. The time-averaged color is $b^{\rm ratio}(r,i) = \bar{f}_\nu(i)/\bar{f}_\nu(r) = 1.53$, so the flux difference spectrum is bluer than the time-averaged spectrum in this object.

correlation coefficient of the $f_\nu(r) - f_\nu(i)$ plot for our sample ($0 < z < 4$) observed more than 20 epochs (see Section 3.5 for more details of our sample). In terms of the Pearson correlation coefficient, almost all of the quasars have strong positive flux−flux correlation. The strong correlation for a quasar light curve means that the flux difference spectrum, which is defined as the flux difference of the quasar spectra of any of the two observational epochs, keeps nearly constant shape for at least several years.

We express a linear regression line ($y = b \times x + a$) in flux−flux space ($f_\nu(s) - f_\nu(l)$ space) as

$$f_\nu(l) = b(s,l) \times f_\nu(s) + a(s,l) \quad (s = u,g,r,i;\ l = g,r,i,z) \tag{1}$$

where "*s*" ("short" wavelength, *x*-axis in flux−flux space), and "*l*" ("long" wavelength, *y*-axis in flux−flux space) indicate two of the five photometric bands, whose average wavelengths are $\lambda(s) < \lambda(l)$ (where $\lambda(u)$, $\lambda(g)$, $\lambda(r)$, $\lambda(i)$, $\lambda(z)$ = 3551, 4686, 6165, 7481, 8931Å)[2]. Figure 3 shows an illustration of our method. When we fit a regression line in flux−flux space, the regression slope $b(s,l)$ and the intercept $a(s,l)$ are expressed as

$$b(s,l) = \frac{\Delta f_\nu^{\rm var}(l)}{\Delta f_\nu^{\rm var}(s)} \tag{2}$$

$$a(s,l) = \bar{f}_\nu(l) - b(s,l)\,\bar{f}_\nu(s) \tag{3}$$

where $\Delta f_\nu^{\rm var}$ is the varying broad-band flux range (flux difference) during the observations, and $\bar{f}_\nu$ is the baseline flux given as the mean flux of light curves for each bandpass. The effects of contaminations of baseline flux (= $\bar{f}_\nu$, e.g., host galaxy flux and time-averaged fluxes of emission lines) do not affect to the regression slope (they only affect to the regression intercepts), so the regression slope in the flux−flux space directly measures the ratio of the two broad-band fluxes of the flux difference spectrum of each quasar.

[2] http://www.sdss.org/dr7/instruments/imager/

Given the flux difference spectrum $f_\nu^{\rm dif}$ for a quasar, the regression slope in flux–flux space is expressed as (Richards et al. 2001),

$$b(s,l) = \frac{\int f_\nu^{\rm dif} S_\nu(l) d\log\nu}{\int f_\nu^{\rm dif} S_\nu(s) d\log\nu} \times \left( \frac{\int S_\nu(l) d\log\nu}{\int S_\nu(s) d\log\nu} \right)^{-1} \quad (4)$$

where $S_\nu$ is the throughput of the SDSS photometric system in each bandpass (Doi et al. 2010).

From Equation (4), the color of the flux difference spectrum $m_s - m_l|_{\rm dif}$ (e.g., $r-i|_{\rm dif}$) in units of magnitude is expressed by $b(s,l)$ as,

$$m_s - m_l|_{\rm dif} = +2.5\log(b(s,l)). \quad (5)$$

This means that the bluer color indicates a smaller value of Equation (5), and then a smaller value of $b(s,l)$. In this way, the color of the flux difference spectrum is related directly to the observable $b(s,l)$. In the present work, we refer $b(s,l)$ simply as "the color of the flux difference spectrum" and this can be converted to the conventional definition of color through Equation (5).

If we assume a power-law difference spectrum ($f_\nu^{\rm dif} \propto \nu^{\alpha_\nu^{\rm dif}}$), we obtain (by Equation (4))

$$b(s,l) \sim \left( \frac{\nu(l)}{\nu(s)} \right)^{\alpha_\nu^{\rm dif}} = \left( \frac{\lambda(s)}{\lambda(l)} \right)^{\alpha_\nu^{\rm dif}} \quad (6)$$

where $\nu(s)$ and $\nu(l)$ indicate average frequencies for the SDSS photometric bands. Because we define $b(s,l)$ as $\lambda(l) > \lambda(s)$,

$$\begin{cases} b(s,l) > 1 & (\text{if } \alpha_\nu^{\rm dif} < 0) \\ b(s,l) < 1 & (\text{if } \alpha_\nu^{\rm dif} > 0). \end{cases} \quad (7)$$

When the flux difference spectra of quasars have power-law shape, the color of the flux difference spectra has no dependence on the quasar redshift because the wavelength-shift by cosmic expansion is canceled out in Equation (6). That is, $b(s,l)$ with a power-law difference spectrum is constant as a function of redshift if $\alpha_\nu^{\rm dif}$ is fixed. Although the color of the difference spectrum is actually contaminated by BEL variability, we can infer $\alpha_\nu^{\rm dif}$ by investigating the mean redshift dependence of $b(s,l)$ for sample quasars.

### 3.2. *The Color of Quasars in Flux-Flux Space*

In flux–flux space, the "observed" color corresponds to the slope of a straight line that passes through the origin of the coordinates and an observed point at an epoch. The "observed" color is time-dependent if $a(s,l)$ (the regression intercept in flux–flux space) is non-zero (Sakata et al. 2010, 2011, and see Appendix B).

We define the $b^{\rm ratio}(s,l)$ by taking the time-average of light curves in any combination of five photometric bands ("baseline flux" $\bar{f}_\nu(j)$, $j = u, g, r, i, z$) and taking the ratio as (see Figure 3)

$$b^{\rm ratio}(s,l) \equiv \frac{\bar{f}_\nu(l)}{\bar{f}_\nu(s)}. \quad (8)$$

Equation (5), which is the (time-averaged) color $m_1 - m_2$ of the quasar spectrum (e.g., $r-i$) is expressed by $b^{\rm ratio}(s,l)$ as

$$m_s - m_l = +2.5\log(b^{\rm ratio}(s,l)). \quad (9)$$

We refer to $b^{\rm ratio}(s,l)$ simply as "the color of the quasar spectrum" in this paper, and you can always convert it to the conventional definition of color through Equation (9).

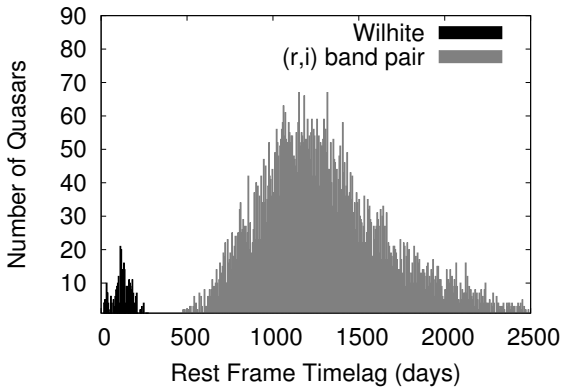


FIG. 4.— Rest-frame time-lag histograms binned for five days. The left histogram (black, median = 123 days) indicates the number of quasars with two-epoch spectra used in Wilhite et al. (2005) (time-lag is defined as the difference of the observational epochs). The right histogram (gray, median $\sim$ 1200 days) is the rest-frame time-lag distribution of *r* and *i*-band light curves, which we used in the present work (time-lag is defined as the difference of first and last observational epochs). See the details of our sample definition in Section 3.5.

$b^{\rm ratio}(s,l)$ is expressed for a quasar with a spectrum $f_\nu$ as

$$b^{\rm ratio}(s,l) = \frac{\int f_\nu S_\nu(l) d\log\nu}{\int f_\nu S_\nu(s) d\log\nu} \times \left( \frac{\int S_\nu(l) d\log\nu}{\int S_\nu(s) d\log\nu} \right)^{-1}. \quad (10)$$

If we assume a power-law spectrum ($f_\nu \propto \nu^{\alpha_\nu}$), we obtain

$$b^{\rm ratio}(s,l) \sim \left( \frac{\nu(l)}{\nu(s)} \right)^{\alpha_\nu} = \left( \frac{\lambda(s)}{\lambda(l)} \right)^{\alpha_\nu}. \quad (11)$$

Because we define $b^{\rm ratio}(s,l)$ as $\lambda(l) > \lambda(s)$,

$$\begin{cases} b^{\rm ratio}(s,l) > 1 & (\text{if } \alpha_\nu < 0) \\ b^{\rm ratio}(s,l) < 1 & (\text{if } \alpha_\nu > 0). \end{cases} \quad (12)$$

### 3.3. *The Color-Redshift Relation*

Richards et al. (2001) investigated the causes of the observed features in the color as a function of redshift for 2625 SDSS quasars by comparing the color–redshift relation model including the effects of emission lines. They confirmed that the average of the observed color of quasars as a function of redshift is well represented by a power-law continuum using $\alpha_\nu \sim -0.5$ (similar to the result of Vanden Berk et al. 2001), and identified the effects of emission lines for the broad-band colors as deviations from power-law colors.

Because we are able to obtain the color of the flux difference spectrum for quasars using the flux–flux correlation method, the same kind of analyses as Richards et al. (2001) for the flux difference spectrum can be applied. Currently, there are only a few studies related to the flux difference spectrum (Wilhite et al. 2005; Bian et al. 2012; Guo & Gu 2013). Among these, we refer to that of Wilhite et al. (2005) for the quasar composite flux difference spectrum in this paper. They constructed the composite residual (composite flux differences spectrum) from 315 quasars observed twice by SDSS spectroscopy. Figure 4 shows the histogram of the rest-frame time-lag between the two spectroscopic observations in Wilhite's sample, with a histogram of the time span of the photometric observations in our sample. The median rest-frame time-lag of the Wilhite's sample is 123 days, which is about one-tenth of ours (median $\sim$ 1200 days). Aside from the difference in the rest-frame time-lag, we can compare our results with the (redshifted) composite flux difference spectrum by

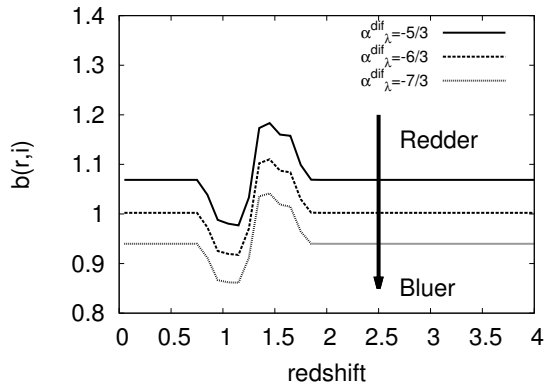


FIG. 5.— Illustration of an emission line contamination effect on the $b(r,i)$–redshift plane. We can treat $b(s,l)$ and $b^{\rm ratio}(s,l)$ in the same way, so here we show the case of $b(s,l)$. Curves are calculated by Equation (4) combined with Equation (13), for $\alpha^{\rm dif}_{\lambda} = -5/3, -6/3, -7/3$. The power-law spectrum with definite spectral index means constant color at all redshift (Equation (6)). At $z \sim 1.1$, the emission line component of Equation (13) enters the *r*-band, and the color becomes bluer than the power-law color. At $z \sim 1.5$, the emission line component leaves the *r*-band and enters the *i*-band, and the color becomes redder than the power-law color.

Wilhite et al. (2005) using Equation (4) on the color–redshift space. Note that Wilhite et al. (2005) mainly focused on the ratio spectrum (the ratio of the composite difference spectrum to the composite spectrum), so they did not apply the correction of Galactic extinction to their composite difference spectrum. We discuss the effect introduced by this non-correction in Section 4.2.

Here, we show the illustration of the effect of an emission line contamination for $b(s,l)$ and $b^{\rm ratio}(s,l)$ on the redshift dependence (see also Richards et al. 2001). We can treat $b(s,l)$ and $b^{\rm ratio}(s,l)$ in the same way, so here we show the case of $b(s,l)$. We consider the case of $s = r$ and $l = i$ (i.e., $b(r,i)$) for example. When an emission line is redshifted and enters *r*-band, the *r*-band flux becomes larger, and $b(r,i)$ becomes smaller (bluer) than the case of a single power-law flux difference spectrum. At higher *z*, when the emission line enters the *i*-band, $b(r,i)$ becomes larger (redder). This behavior is shown in Figure 5, assuming the continuum and line variability as

$$\begin{aligned} f^{\rm dif}_{\lambda} &= f^{\rm dif}_{\lambda}({\rm continuum}) + f^{\rm dif}_{\lambda}({\rm line}) \\ &= \left(\frac{\lambda}{3000\text{Å}}\right)^{\alpha^{\rm dif}_{\lambda}} + \frac{1}{2}\exp\left(-\frac{(\lambda-\lambda_{\rm rest})^2}{2\sigma^2_{\lambda}}\right) \end{aligned} \quad (13)$$

where $\sigma_{\lambda}$ is the emission line width (here $\sigma_{\lambda} = 40$Å), and $\lambda_{\rm rest}$ is the central wavelength of the line (here $\lambda_{\rm rest} = 3000$Å). $\alpha^{\rm dif}_{\lambda}$ is as shown in Figure 5. The different power-law indices $\alpha^{\rm dif}_{\lambda}$ lead to the different constant levels of $b(s,l)$ following Equation (6).

### 3.4. *Advantages of the Flux-Flux Correlation Method*

Schmidt et al. (2012) pointed out that previous analyses usually focused on the color variability of the quasar in color–magnitude space and suffered from covariance between the color and magnitude uncertainties. They avoided these error correlations by analyzing the color variability in magnitude–magnitude space, and concluded that the color variability has the bluer-when-brighter trend.

Although magnitude–magnitude correlation method can avoid error correlations, it still has another problem. Schmidt et al. (2012) fitted a straight line for each quasar's magnitude–magnitude plot, and used the best fit slope as the indicator of color variability. Note that regression slopes on magnitude–magnitude space highly depend on the contaminations of baseline flux (e.g., host galaxy flux and time-averaged fluxes of emission lines) (e.g., Woo et al. 2007; Hawkins 2003). The regression slope in magnitude–magnitude space can be expressed as

$$b^{\rm mag}(s,l) \approx \frac{\log[\left(\bar{f}_{\nu}(l)+\Delta f^{\rm var}_{\nu}(l)/2\right)/\left(\bar{f}_{\nu}(l)-\Delta f^{\rm var}_{\nu}(l)/2\right)]}{\log[\left(\bar{f}_{\nu}(s)+\Delta f^{\rm var}_{\nu}(s)/2\right)/\left(\bar{f}_{\nu}(s)-\Delta f^{\rm var}_{\nu}(s)/2\right)]}$$

where the notation is the same as Equation (2) and (3). Unlike in flux–flux space (Equation (2)), the regression slope in magnitude-magnitude space is dependent not only on the flux difference $\Delta f^{\rm var}_{\nu}$, but also on the time-averaged flux levels $\bar{f}_{\nu}$ ("baseline flux", Equation (8)). Thus, $b^{\rm mag}(s,l)$ only tells whether the "observed" color variability is bluer-when-brighter ($b^{\rm mag} < 1$), redder-when-brighter ($b^{\rm mag} > 1$) or achromatic ($b^{\rm mag} = 1$). To derive the flux difference spectrum from $b^{\rm mag}$, one needs to employ some models or estimate the contamination $\bar{f}_{\nu}$. On the other hand, the flux–flux correlation method enables us not only to avoid error correlations, but also to derive the flux difference spectrum model independently (Equation (2)).

Another statistical method to derive the flux difference spectrum exists. Meusinger et al. (2011) investigated the rest-frame wavelength dependence of the quasar variability using the structure functions $V^{\rm mag}$ of five SDSS photometric bands as a function of rest-frame wavelength. However, the structure function analyses, which are done in units of magnitude, are not appropriate to study the spectral variability or the flux difference spectrum because the structure function can be expressed as

$$\begin{aligned} V^{\rm mag} &\approx [\Delta m]^2 \\ &\approx \left[-2.5\log\left(\frac{\bar{f}_{\nu}(s)+\Delta f^{\rm var}_{\nu}(s)/2}{\bar{f}_{\nu}(s)-\Delta f^{\rm var}_{\nu}(s)/2}\right)\right]^2. \end{aligned}$$

Then again, this is dependent not only on the flux difference $\Delta f^{\rm var}_{\nu}$, but also on the time-averaged flux levels $\bar{f}_{\nu}$.

In summary:

1. The flux–flux correlation method can avoid the error correlations that exist in magnitude–color or flux–color correlation method as was pointed out by Schmidt et al. (2012).

2. The regression slope $b(s,l)$ derived by the flux–flux correlation of a quasar multi-band light curve is not affected by baseline fluxes (e.g., host galaxy flux or time-averaged fluxes of emission lines).

3. Regression slopes represent the color of the flux difference spectrum for each quasar, so we are able to infer the (mean) flux difference spectrum using redshift dependence of the derived regression slopes.

### 3.5. *Linear Regression Method and Sample Selection*

Linear regression for the data that have intrinsic scatter ($\sigma_{\rm int}$) and error bars on both axes (e.g., flux–flux space linear regression) is complex and there are several different methods (see Park et al. 2012; Feigelson & Jogesh Babu 2012; Cappellari et al. 2013, and references therein). We adopt the

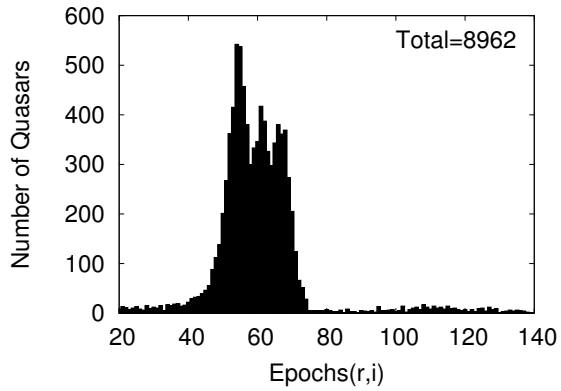


FIG. 6.— Histogram of the number of observational epochs of the ($r$,$i$) band pair light curves for our quasar sample. Observations with a "Bad observations" flag (MacLeod et al. 2012) are excluded.

MPFITEXY IDL routine (Williams et al. 2010) to fit a linear relation to the flux–flux correlation for each quasar. According to Park et al. (2012), the FITEXY method generally provides the least-biased result compared to the other methods. The MPFITEXY routine depends on the MPFIT package (Markwardt 2009). This routine is able to cope with intrinsic scatter, which is automatically adjusted to ensure $\chi^2$/(degrees or freedom) $\sim$1 (see Tremaine et al. 2002; Novak et al. 2006; Park et al. 2012, for more detail and justifications).

We fit a straight line in flux–flux space for each band pair light curve, excluding the data points with a "Bad observations" flag (MacLeod et al. 2012) or fainter than limiting magnitudes (22.0, 22.2, 22.2, 21.3, and 20.5mag for $u$, $g$, $r$, $i$, and $z$-band, respectively).[3] We focused on the properties of long-term and multi-epoch-averaged variability, so we exclude quasars that have less than 20 photometric epochs. Linear relation $y = b(x-x_0)+a'$ is assumed in the fitting procedure, where $x_0$ is taken to be the average of $x$ values (i.e., $\bar{f}_\nu(s)$). The reference value $x_0$ is necessary to minimize the uncertainty in the estimate of $a'$ and the correlation between $a'$ and $b$ (Tremaine et al. 2002). Regression intercept $a$ is calculated as $a = a' - bx_0$. Linear regression for several quasars did not converge because of the low signal-to-noise ratio (S/N). Thus, we eliminated them from our sample. Furthermore, we confirmed that all of the regression slopes with a negative value were the results of a bad fitting (because of the small variability or low S/N) and we also eliminated them from our sample. In this paper we examine the modal redshift trends, so these eliminations had little effect on our analyses.

As an example, we show the histogram of the number of observational epochs of the ($r$,$i$) band pair light curves without a "Bad observations" flag (MacLeod et al. 2012) for our quasar sample in Figure 6. Resulting sample sizes for each band pair are shown in Table 1. Redshift distribution is not significantly modified from Figure 1 by our sample selection.

TABLE 1
SAMPLE SIZE
($0 < z < 4$)

| $(s,l)$ | Samples |
|---|---|
| $(u,g)$ | 8,537 |
| $(u,r)$ | 8,523 |
| $(u,i)$ | 8,495 |
| $(u,z)$ | 8,213 |
| $(g,r)$ | 8.996 |
| $(g,i)$ | 8,949 |
| $(g,z)$ | 8,745 |
| $(r,i)$ | 8,962 |
| $(r,z)$ | 8,770 |
| $(i,z)$ | 8,761 |

## 4. CONTINUUM VARIABILITY

In this section, we show linear regression slopes $b(s,l)$ derived in flux–flux space for quasar light curves, which correspond to the color of the flux difference spectrum as discussed in the previous section. The wide redshift range for our quasar samples and large separation of effective wavelengths of the SDSS filters enable us to investigate the continuum variability from 1216Å to about 6000Å in the rest-frame wavelength. We first check the consistency between our result and the previous spectroscopic result of the flux difference spectrum (Wilhite et al. 2005). Then, we adopt a model for the continuum flux variation in which the variability is caused by changes in mass accretion rate in the standard accretion disk (Pereyra et al. 2006) as a working hypothesis, and compare it with observed continuum variability in $b(s,l)$–redshift space.

### 4.1. *Redshift Dependence of the Color of the Flux Difference Spectrum*

Figure 7 shows the regression slopes $b(s,l)$ as a function of redshift for each quasar (dots). The curves in Figure 7 are:

- Solid and dashed curves: The modal color ($b(s,l)$) of the flux difference spectrum (solid) with $1\sigma$ outer quartiles (dashed), derived by linear regression analyses in flux–flux space (i.e., mode and $1\sigma$ outer quartiles of the dots in the figure).

- Dash-dotted and double-dot-dashed curves: The modal color ($b^{\rm ratio}(s,l)$) of the time-averaged spectrum (dash-dotted) with $1\sigma$ outer quartiles (double-dot-dashed), given by Equation (8).

Modal value is defined following Hopkins et al. (2004), and the bin size is taken to be 0.2 in redshift.

At high redshift, $u$, $g$, and $r$-band fluxes are affected by Ly$\alpha$ forests or damped Ly$\alpha$ systems, which absorb UV flux and decrease $u$, $g$, and $r$-band variability (i.e., regression slopes become larger at higher redshifts). This makes it difficult to estimate intrinsic quasar spectrum and spectral variability. The shortest transmission wavelengths for $u$, $g$, and $r$-band are 3000Å, 3700Å, and 5400Å, respectively, so the Ly$\alpha$ emission line (1216Å) enters in these bands at $z = 1.47, 2.04, 3.44$. The arrows with the label "Ly$\alpha$" in Figure 7 indicate the redshift ranges in which Ly$\alpha$ forests change the observed color. In the later sections, we focus on redshift range below $z = 1.47$, 2.04, and 3.44 for band pairs containing $u$, $g$, and $r$-band, respectively, for clarifying the discussion about intrinsic spectral variability.

The dash-dotted curves ($b^{\rm ratio}(s,l)$) in Figure 7 are generally larger than 1. This is consistent with the result of the geometric mean composite spectrum for SDSS quasars presented by Vanden Berk et al. (2001); the spectral index of the composite spectrum $\alpha_\nu^{\rm com} \sim -0.44 < 0$ ($\alpha_\lambda^{\rm com} \sim -1.56$) indicates $b(s,l) > 1$ (Equation (12)). The upper thin solid horizontal line in each panel of Figure 7 indicates the power-law spectrum model with $\alpha_\nu = -0.44$ calculated by Equation (4).

[3] http://www.sdss.org/dr7/

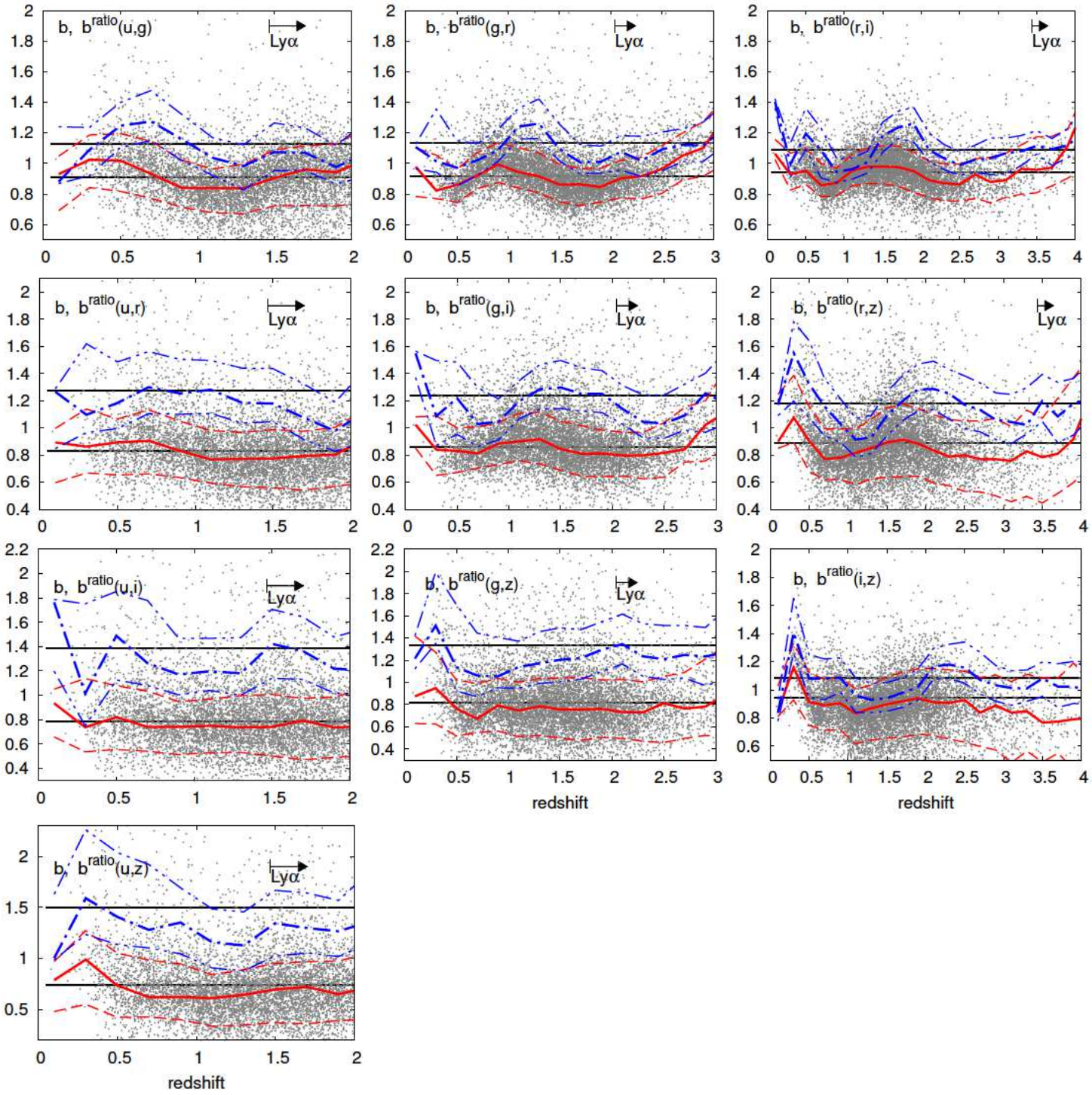


FIG. 7.— Regression slopes $b(s,l)$ as a function of redshift (dots). Solid curves with dashed outer quartiles (colored red in the electronic edition) indicate the mode and the $1\sigma$ (68%) range of the slopes for each redshift bins ($\Delta z = 0.2$), and dash-dotted curves with double-dot-dashed outer quartiles (colored blue in the electronic edition) are the mode of the ratio of fluxes $b^{\rm ratio}(s,l)$ defined by Equation (8). Two thin horizontal lines (upper and bottom) indicate the case of power-law spectrum models, $\alpha_\nu = -0.44$ and $+1/3$ ($\alpha_\lambda = -1.56, -7/3$), respectively. $b^{\rm ratio}(s,l)$–redshift relation (i.e., the color of the time-averaged observed spectrum as a function of redshift) can be represented by $\alpha_\nu^{\rm com} = -0.44$ (Vanden Berk et al. 2001). On the other hand, $b(s,l)$–redshift relation (i.e., the color of the difference spectrum as a function of redshift) can be represented by $\alpha_\nu^{\rm dif} = +1/3$.

On the other hand, the solid curves ($b(s,l)$) in Figure 7 are generally less than 1 and it implies $\alpha_\nu^{\rm dif} > 0$ (Equation (7)). The composite flux difference spectrum presented by Wilhite et al. (2005) was reported to have the spectral index $\alpha_\nu^{\rm dif} = 0$, and it implies $b(s,l) = 1$ (Equation (6)). However, the solid curves in Figure 7 are less than 1 within the $1\sigma$ ranges (dashed curves). We attempt to employ the spectral index $\alpha_\nu^{\rm dif} = +1/3$ that is suggested by Sakata et al. (2010) (the lower thin, solid horizontal line in each panel of Figure 7). This spectral index seems to reproduce the mean value of the $b(s,l)$ for all the band pairs well. This inconsistency between the result of Wilhite et al. (2005) and ours is discussed in Sec-

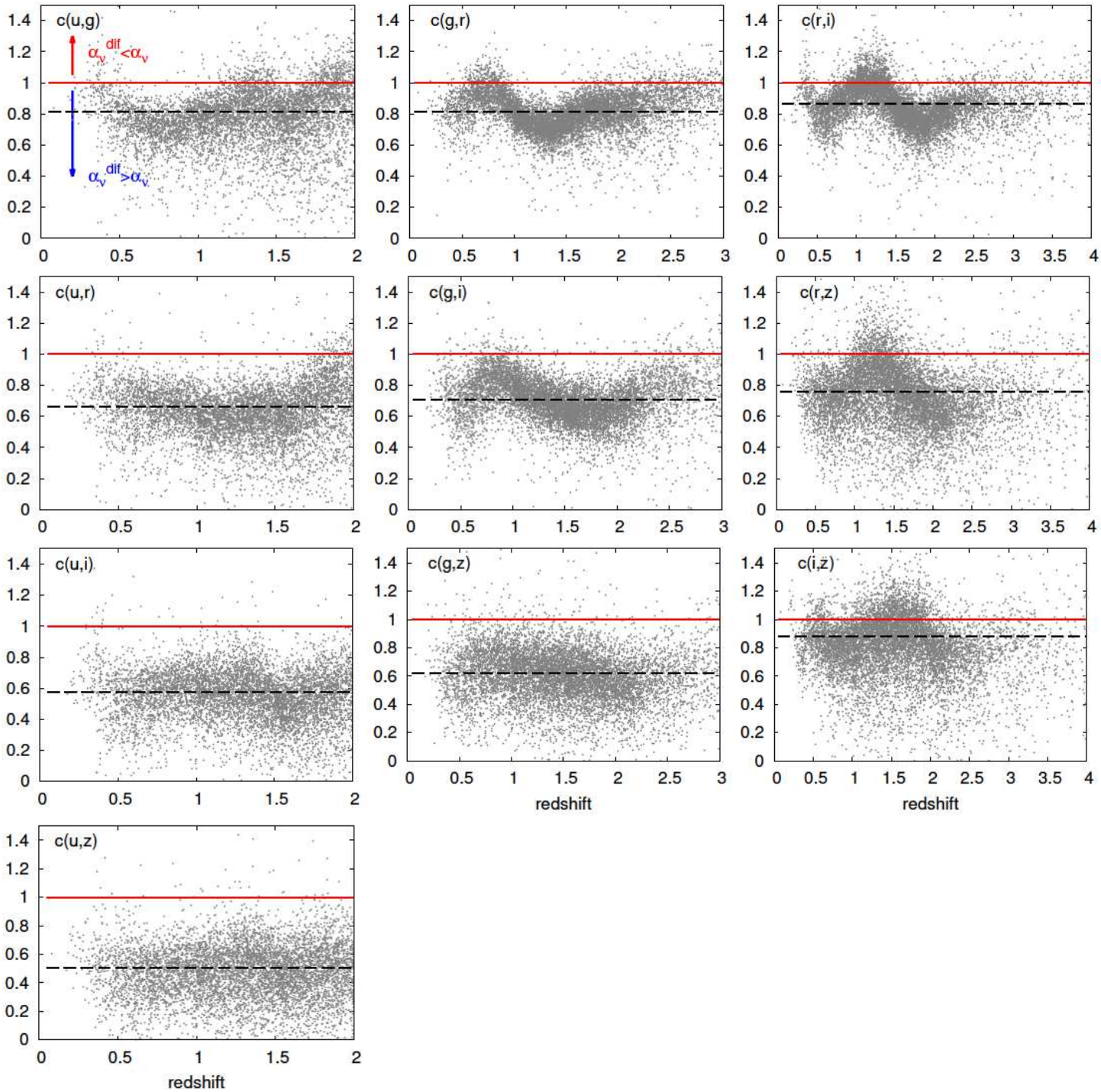


FIG. 8.— $c(s,l) \equiv b(s,l)/b^{\rm ratio}(s,l)$ (Equation (14)) as a function of redshift. The dashed horizontal lines indicate $\Delta\alpha_\nu = \alpha_\nu^{\rm dif} - \alpha_\nu = -\alpha_\lambda^{\rm dif} + \alpha_\lambda = +7/3 - 1.56 \sim 0.77$ (difference of the spectral indices shown in Figure 7), and the solid lines (colored red in the electronic edition) indicate $\Delta\alpha_\nu = 0.0$. $c(s,l) > 1$ implies $\alpha_\nu^{\rm dif} < \alpha_\nu$ (corresponds to redder-when-brighter trend in observed color), and $c(s,l) < 1$ implies $\alpha_\nu^{\rm dif} > \alpha_\nu$ (corresponds to bluer-when-brighter trend in observed color).

tion 4.2.

$b^{\rm ratio}(s,l) > b(s,l)$ is the general trend for quasar variability as shown in Figure 7 (see also Appendix B). This indicates that the quasar composite flux difference spectrum is flatter (bluer) than the composite spectrum. In other words, quasar UV–optical spectra tend to become flatter (bluer) when in brighter phase. To clarify the "observed" bluer-when-brighter trend for individual quasars, we show the ratio of $b(s,l)$ to $b^{\rm ratio}(s,l)$ given as

$$c(s,l) \equiv \frac{b(s,l)}{b^{\rm ratio}(s,l)} \sim \left(\frac{\lambda(s)}{\lambda(l)}\right)^{\Delta\alpha_\nu} \qquad (14)$$

as a function of redshift in Figure 8, where $\Delta\alpha_\nu = \alpha_\nu^{\rm dif} - \alpha_\nu$ (approximate value is from Equation (6) and (11)). By defini-

tion, as in Equation (7) and (12),

$$\begin{cases} c(s,l) > 1 & (\text{if } \alpha_\nu^{\rm dif} < \alpha_\nu) \\ c(s,l) < 1 & (\text{if } \alpha_\nu^{\rm dif} > \alpha_\nu). \end{cases} \quad (15)$$

Dashed horizontal lines in Figure 8 indicate $\Delta\alpha_\nu = \alpha_\nu^{\rm dif} - \alpha_\nu = -\alpha_\lambda^{\rm dif} + \alpha_\lambda = 7/3 - 1.56 \sim 0.77$ (difference of the spectral indices shown in Figure 7), and solid horizontal lines indicate the case of $\alpha_\nu^{\rm dif} = \alpha_\nu$. Figure 8 shows that almost all of quasars have $\alpha_\nu^{\rm dif} > \alpha_\nu$. This means the "observed" bluer-when-brighter spectral variability is a common trend in quasars.

Besides the continuum (power-law) variability, we are able to see several spectral features in Figure 7 and also in Figure 8. These features are mainly made up of the emission line contributions (e.g., Wilhite et al. 2005). It is known that the emission line variability is smaller compared with the continuum variability (intrinsic Baldwin effect, Wilhite et al. 2005). As expected by the intrinsic Baldwin effect, the solid curves in Figure 7 show less features compared to the dash-dotted curves. Nonetheless, we are still able to identify the coincidence and the difference of features (the redshift dependence) between the solid and dash-dotted curves. The most apparent difference between them, which corresponds to the difference between the composite and composite difference spectrum, is the bump in intermediate redshifts (e.g., the redshift range $z \sim$ 1.0-1.5 of $g-r$ band pair in Figure 7). This difference makes several sharp transitions on $c(s,l)$ as a function of redshift shown in Figure 8. The peaks of the bump of dash-dotted curves correspond to the spectral region of Mg II (2800Å) emission line and Fe II pseudo-continuum, and this peak is not seen in the solid curves. It implies that the variability of these emissions are weak. This point is discussed in Sections 5 and 6.

### 4.2. *Comparison with the Composite and Composite Difference Spectrum*

There have been several statistical studies about spectral shape and spectral variability for quasars selected and spectroscopically confirmed within SDSS. Here we show the consistency of these previous spectroscopic results with our photometric results.

Figure 9 shows the comparison of our results (modal color as a function of redshift in Figure 7) with the composite (Vanden Berk et al. 2001) and composite difference (Wilhite et al. 2005) spectrum using Equation (10) and (4). In Figure 9 we plot not only modal value, but also (weighted) mean value as a function of redshift to check the effects of the asymmetric color distribution, which has a red wing at a given redshift due to intrinsic dust reddening (Richards et al. 2003). We are able to see in Figure 9 that the mean values are slightly larger (redder) than the modal value, but the difference is small. This indicates that our results are not affected heavily by this method of taking average.

The composite spectra composed by taking arithmetic or geometric means (Vanden Berk et al. 2001; Wilhite et al. 2005) are compared with our result through Equation (4) and (10). The geometric mean preserves the average power-law slope, insofar as quasar spectra can be accurately described by a power-law. On the other hand, the arithmetic mean retains the relative strength of the non-power-law features, such as emission lines (Vanden Berk et al. 2001).

As shown in the top panel of Figure 9, $b^{\rm ratio}(r,i)$ of our result and of the composite spectrum (Vanden Berk et al. 2001) are generally consistent. Vanden Berk et al. (2001) presented

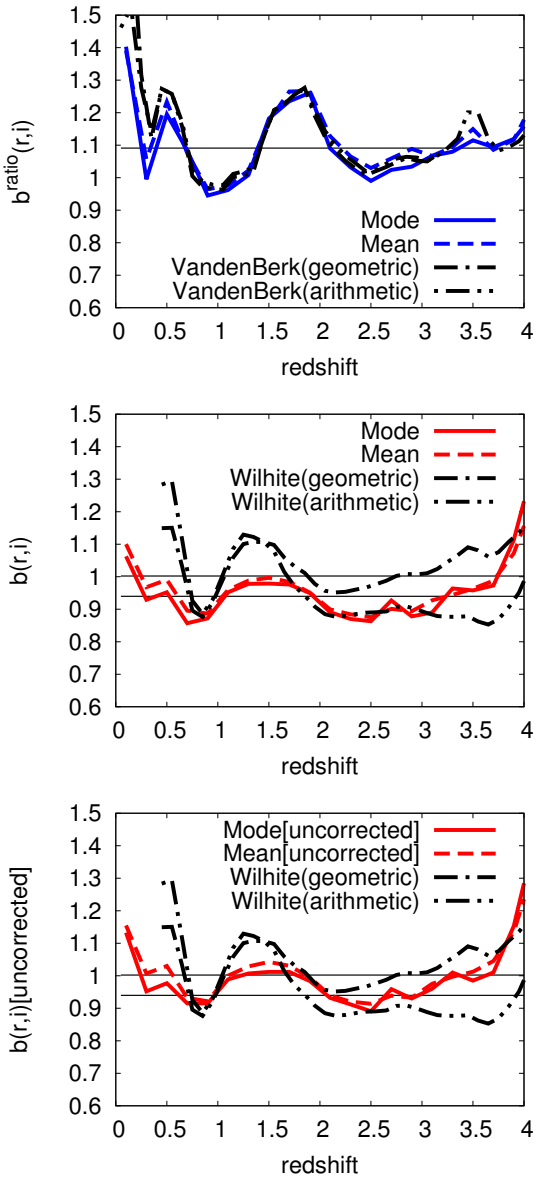


FIG. 9.— Top panel: the comparison of the modal and mean color of the time-averaged spectrum ($b^{\rm ratio}(r,i)$) with the color of the redshifted geometric and arithmetic composite spectrum (Vanden Berk et al. 2001) calculated by Equation (10). The horizontal line is the color of a power-law spectrum with $\alpha_\nu$ = –0.44 (Vanden Berk et al. 2001). Middle panel: the comparison of the modal and mean color of the difference spectrum ($b(r,i)$) with the color of the redshifted geometric and arithmetic composite difference spectrum (Wilhite et al. 2005) calculated by Equation (4). The two horizontal lines are the color of power-law difference spectra with $\alpha_\nu^{\rm dif}$ = 0 and +1/3 (upper and lower, respectively). Bottom panel: the same plot as middle panel, but the modal and mean color of the difference spectrum ($b(r,i)$) is not corrected for Galactic extinction.

the geometric and arithmetic composite spectra, but their difference is very small (their spectral index is $\alpha_\nu$ = –0.44 and –0.46, respectively, with the uncertainty $\sim$ 0.1 due to the spectrophotometric calibration) and they have almost the same $b^{\rm ratio}(r,i)$–redshift relation. Power-law index $\alpha_\nu$ = –0.44 (shown as dotted line in upper panel of Figure 9) is consistent with $b^{\rm ratio}(r,i)$, and as we have shown in Figure 7, all $b^{\rm ratio}(s,l)$ are also consistent with $\alpha_\nu$ = –0.44.

On the other hand, $b(r,i)$ of the regression results and the geometric composite difference spectrum (Wilhite et al. 2005) (middle panel of Figure 9) seem to be inconsistent in

that $b(r,i)$ of the regression results are generally lower than that of the composite difference spectrum for any redshift. This indicates that their composite geometric difference spectrum is steeper than our sample mean color of the difference spectra. We note that their difference spectra composed by taking geometric mean and arithmetic mean are largely different. The authors did not specify the reasons for this large discrepancy. They rely on the geometric composite spectrum when inferring the continuum spectral index $\alpha_\nu^{\rm dif} = 0.0$, and we should compare our result with the geometric one when inferring the continuum variability. Also, we note that their spectra are not corrected for Galactic extinction (see Abazajian et al. 2004; Wilhite et al. 2005). The composite spectra with no correction for Galactic extinction obtained by Wilhite et al. (2005) has the spectral index $\alpha_\lambda^{\rm com} = -1.35$, which is steeper (redder) than the dereddened composite spectrum by Vanden Berk et al. (2001) ($\alpha_\lambda^{\rm com} = -1.56$). So, the composite flux difference spectrum with $\alpha_\lambda^{\rm dif} = -2.0$ with no correction for Galactic extinction obtained by (Wilhite et al. 2005) means that the intrinsic composite flux difference spectrum should have flatter (bluer) spectral index (i.e., $\alpha_\lambda^{\rm dif} < -2.0$), which is consistent with our result $\alpha_\lambda^{\rm dif} \sim -7/3$ or $\alpha_\nu^{\rm dif} \sim +1/3$. In the bottom panel of Figure 9 we show $b(r,i)$ with no correction for Galactic extinction as a function of redshift. In this plot, although bumpy features in the $b(r,i)$–redshift relation (which correspond to the emission lines variability and are discussed in Sections 5 and 6) of the regression results are still not in good agreement with that of the geometric composite difference spectrum (Wilhite et al. 2005), it is clear that our result and that of the geometric composite difference spectrum (Wilhite et al. 2005) are approximately consistent in that they have similar average power-law value. Thus, a large fraction of the discrepancy between our result and that of Wilhite et al. (2005) seen in the middle panel of Figure 9 can be attributed to a correction or no-correction for the Galactic extinction. It also indicates that the composite flux difference spectrum is not so different in spite of the large difference in time scale between ours and that of (Wilhite et al. 2005, ; see Figure 4).

Hereafter, we refer the approximate form of power-law continuum flux difference spectrum as

$$f_\nu^{\rm dif} \propto \nu^{+1/3} \tag{16}$$

(i.e., $\alpha_\nu^{\rm dif} \sim +1/3$). This power-law index is well known as the standard disk model prediction (Lynden-Bell 1969; Shakura & Sunyaev 1973). Tomita et al. (2006) and Lira et al. (2011) concluded that the flux difference spectra in near infrared (NIR) wavelengths for their AGN samples are well represented by a combination of the dusty torus component (Blackbody spectrum) and the accretion disk component ($\alpha_\nu^{\rm dif} \sim +1/3$) on the assumption that the flux difference spectrum conserves the spectral shape (spectral index) of the underlying accretion disk spectrum (see also Paltani & Walter 1996; Collier et al. 1999). Note that the observations of the polarized flux spectra of AGNs – which is assumed to be produced by electron scattering interior to the dust sublimation radius and is regarded as a copy of the spectrum originating in the accretion disk – also revealed the underlying continuum spectral shape consistent with $\alpha_\nu = +1/3$ ($\alpha_\nu = +0.44 \pm 0.11$, Kishimoto et al. 2008). Our result can be considered to be the UV–optical extension of the previous results on the flux difference spectrum obtained in the optical–NIR wavelengths (Tomita et al. 2006; Lira et al. 2011), because the dust in the nuclear region cannot become higher temperature than the dust sublimation temperature ($T_{\rm sub} \sim 1500$K) and the accretion disk component dominate in UV–optical wavelengths.

In Section 4.3, we discuss the validity of the accretion disk model in UV–optical wavelengths.

### 4.3. *Comparison with Standard Accretion Disk Model*

Pereyra et al. (2006) fitted the composite flux difference spectrum presented by Wilhite et al. (2005) with a standard thermal accretion disk model (Shakura & Sunyaev 1973), in which the luminosity varies following the changes in accretion rate from one epoch to the next, and concluded that most of the UV–optical variability observed in quasars may be due to processes involving changes in mass accretion rates. Sakata et al. (2011) investigated this model for 10 SDSS quasars individually, and also concluded that the model can explain the UV-optical variability quantitatively. Definitions of the model adopted by Pereyra et al. (2006) and Sakata et al. (2011) are slightly different in that the former depends on the first order Taylor expansion about the average characteristic temperature $T^*$ (see Pereyra et al. 2006), but the predicted flux difference spectra are identical for the modest variation amplitude, which is valid for most of quasars.

In the formalization of Pereyra et al. (2006), the model flux difference spectrum has two free parameters: a normalization constant and the average characteristic temperature $T^*$. One of the advantages of focusing on the color–redshift relation is that it does not depend on the inclination angle (including limb-darkening effect, e.g., Phillips & Meszaros 1986). When inferring the color of the flux difference spectrum (observable $b(s,l)$ in the present work), this model requires only one parameter $T^*$ because the normalization constant does not affect the color of the difference spectrum. $T^*$ is defined as

$$T^* = \left( \frac{3GM_{\rm BH}\dot{M}}{8\pi\sigma_S (3R_S)^3} \right)^{1/4} \tag{17}$$

$$= 90,600{\rm K} \left( \frac{\epsilon}{1/12} \right)^{-1/4} \left( \frac{M_{\rm BH}}{10^9 M_\odot} \right)^{-1/4} \left( \frac{\rm ER}{0.1} \right)^{1/4} \tag{18}$$

where $M_{\rm BH}$ is the black hole mass, $\dot{M}$ is the mass accretion rate, $\sigma_S$ is the Stefan-Boltzmann constant, and K denotes the kelvin. The disk inner edge is assumed to be at the inner stable circular orbit ($R_{\rm in} = 3R_S$, where $R_S$ is Schwarzschild radius). Eddington luminosity is defined as $L_{\rm Edd} = 4\pi G M_{\rm BH} m_p c/\sigma_T$ (where $m_p$ is the proton mass and $\sigma_T$ is the Thomson cross section) and Eddington ratio, denoted "ER", is given as ER $\equiv L_{\rm bol}/L_{\rm Edd}$. Radiative efficiency $\epsilon$, defined as $L_{\rm bol} = \epsilon \dot{M} c^2$, is fixed[4] to $\epsilon = 1/12$. Changes in $\dot{M}$ lead to the changes in $T^*$ as $T^* \propto \dot{M}^{1/4}$ and then to the changes in flux. Pereyra et al. (2006) fitted their continuum variability model to the geometric mean flux difference spectrum of Wilhite et al. (2005), and obtained $T^* = 92,700$ K. The upper panel of Figure 10 shows the characteristic temperature of our quasar samples calculated by Equation (18) using the fiducial virial black hole mass and Eddington ratio listed in quasar property catalog (Shen et al. 2011). $T^* = 92,700$ K, obtained by Pereyra et al. (2006), is very reasonable for SDSS quasars.

This model predicts $\alpha_\nu^{\rm dif} = 1/3$ around optical to near infrared wavelengths (e.g., Sakata et al. 2010). This spectral in-

[4] In the (non-relativistic) standard disk model, the radially integrated disk luminosity is $L_{\rm bol} = (GM_{\rm BH}\dot{M})/(2R_{\rm in}) = (1/12)\dot{M}c^2$, then $\epsilon = 1/12$ (Kato et al. 2008).

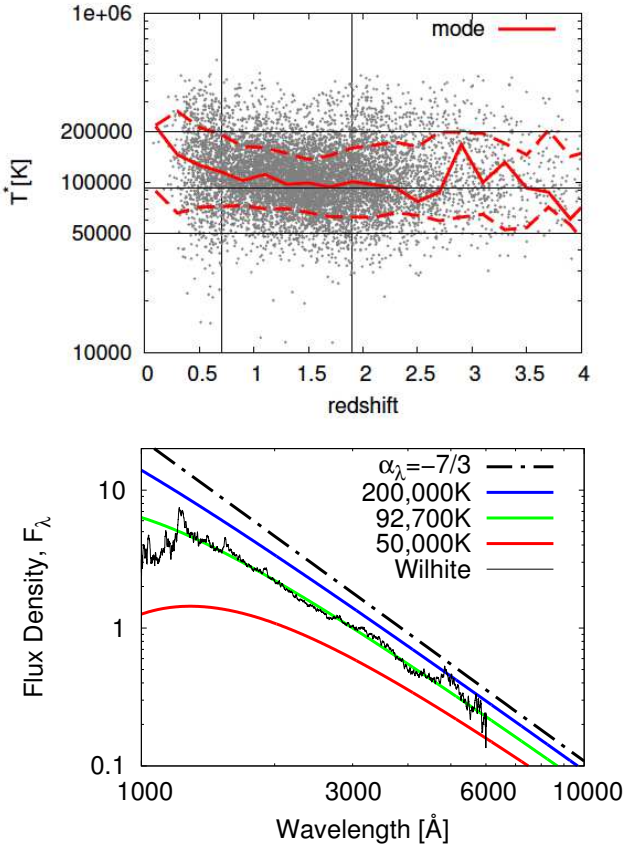


FIG. 10.— Upper panel: characteristic temperature of SDSS Stripe 82 quasars calculated by Equation (18) with the use of a quasar property catalog (Shen et al. 2011). Vertical thin solid lines indicate redshift ranges in which bolometric luminosities are computed in different ways: from $L_{5100}$ ($z < 0.7$), $L_{3000}$ ($0.7 < z < 1.9$), $L_{1350}$ ($z > 1.9$) using bolometric corrections $BC_{5100} = 9.26$, $BC_{3000} = 5.15$, and $BC_{1350} = 3.81$, respectively (Shen et al. 2011). A horizontal thin solid line indicates $T^* = 200{,}000$ K, 92,700 K (best-fit value obtained by Pereyra et al. 2006), 50,000 K. The solid curve with dashed outer quartiles (colored red in the electronic edition) indicate the mode and the $1\sigma$ range for each redshift bin ($\Delta z = 0.2$). Bottom panel: model flux difference spectra $f_\nu^{\rm dif}$ (Pereyra et al. 2006), calculated for $T^* = 200{,}000$ K (bluest), $92{,}700$ K, and $50{,}000$ K (reddest). A dash-dotted line is a power-law with $\alpha_\lambda = -7/3$. For comparison, the geometric composite flux difference spectrum by Wilhite et al. (2005) is shown as a thin line. Spectra are arbitrarily scaled.

dex is well known as the long wavelength limit for a standard thermal accretion disk model (Shakura & Sunyaev 1973). At the long wavelength limit, the accretion disk model spectrum with varying accretion rate turns out to be simple scaling, thus the flux difference spectrum predicted in this model also has $\alpha_\nu^{\rm dif} \sim +1/3$. Because we obtained $\alpha_\nu^{\rm dif} \sim +1/3$ as shown in Figure 7, this model is approximately valid. However, we should be careful because:

- The long wavelength limit approximation is not valid for the wavelength range of SDSS photometry for high-redshift quasars. In UV wavelengths, $f_\nu^{\rm dif}$ predicted by this model becomes gradually steeper (redder) because the UV spectral range corresponds to the turnover spectral region of the blackbody radiation from the accretion disk inner boundary at the inner stable circular orbit (i.e., the hottest part of the disk), as seen in the lower panel of Figure 10.

- Pereyra et al. (2006) used the composite difference spectrum not corrected for Galactic extinction (Wilhite et al. 2005), and the effect of the non-correction is not investigated in their paper. The same is true for Sakata et al. (2011), in which the correction for the Galactic extinction was not properly applied.[5] It is possible that the non-correction for Galactic extinction leads to the wrong conclusion.

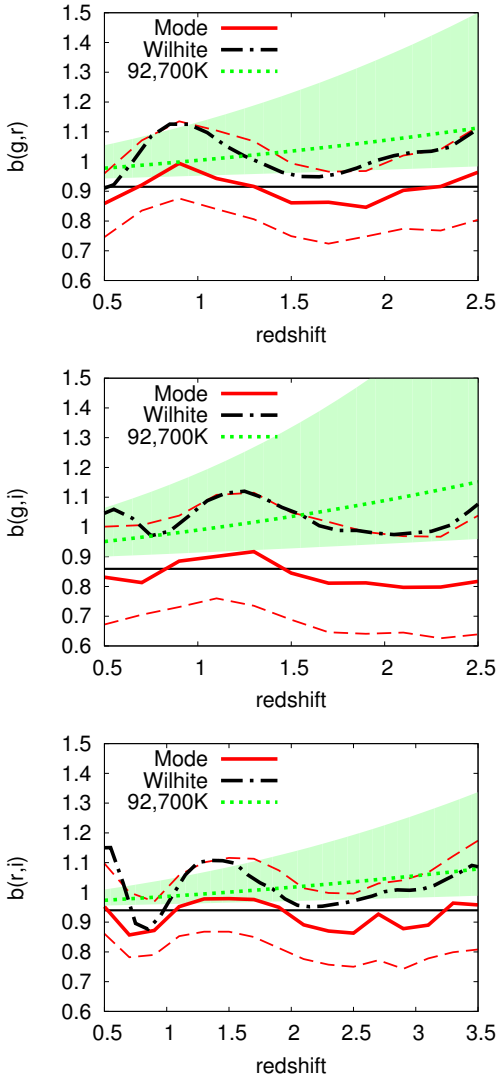


FIG. 11.— Comparison of the observed $b(s,l)$ (corrected for Galactic extinction) with prediction by a standard thermal accretion disk model (Pereyra et al. 2006) in $b(s,l)$-redshift space. Dotted curves (colored green in the electronic edition) indicate a standard thermal accretion disk model with changing mass accretion rate, assuming that the average characteristic disk temperature is $T^* = 92{,}700$K (Pereyra et al. 2006). The filled region (colored light green in the electronic edition) corresponds to the disk temperature ranges from $T^*$ =50,000 K to 200,000 K (see Figure 10). The solid curves with dashed outer quantile (colored red in the electronic edition) are the same as those in Figure 7. The dash-dotted curves are calculated from the geometric composite flux difference spectrum (the same as those in Figure 9). Horizontal thin solid lines are the color of the power-law difference spectrum with $\alpha_\nu^{\rm dif} = +1/3$.

So, it is worth comparing our (Galactic-extinction corrected) result with the model prediction to clarify the validity of the standard disk model. We compare our results with

[5] Sakata et al. (2011) mentioned that they used the point-spread function magnitude corrected for Galactic extinction obtained from the SDSS database, but we found that the light curves shown in their figures are not properly corrected for it.

the model proposed by Pereyra et al. (2006) in $b(r,i)$–redshift space as shown in Figure 11. In Figure 11, Pereyra's model (with their best-fit value of $T^*$ =92,700K) is actually in agreement with the Wilhite's composite flux difference spectrum. However, the model prediction is apparently steeper ($b(r,i)$ is larger) than our result. This discrepancy is mainly due to whether or not Galactic extinction is corrected (see middle and bottom panel in Figure 9). In Figure 11, we also plot the model prediction range in $b(s,l)$-redshift space, which is from $T^* = 50,000$ K (upper boundary) to $200,000$ K (lower boundary). The model prediction is apparently not consistent with the $b(s,l)$–redshift region obtained in our analyses, in that the model predicts larger $b(s,l)$ values and larger spread in $b(s,l)$–redshift space than observed values particularly in the high redshift range.

These indicate that the intrinsic composite flux difference spectrum of quasars is actually flatter (bluer) than the prediction of the accretion disk model, particularly in the UV wavelength range. In other words, we cannot see the model-predicted "UV turnover" feature (e.g., Shang et al. 2005) in the flux difference spectrum. This result is qualitatively consistent with Schmidt et al. (2012), but our method enables us to examine the difference between observed variability and the model prediction quantitatively.

We are able to make the model flux difference spectrum flatter (up to $f_\nu^{\rm dif} \propto \nu^{1/3}$ at all UV–optical wavelengths) if we assume the disk characteristic temperature to be , for example, $T^* > 200,000$ K, but this is not valid for most of our quasar samples as shown in the upper panel of Figure 10. Beyond the standard accretion disk model (Shakura & Sunyaev 1973), several more sophisticated accretion disk models are proposed (see, e.g., Hubeny et al. 2000; Davis et al. 2007). However, accretion disk model spectra based on non-LTE atmosphere calculations (Davis et al. 2007) usually have redder color than the standard thermal accretion disk model because of opacity effects (e.g., Hubeny et al. 2000) and this leads to the redder color of the flux difference spectrum as shown in Schmidt et al. (2012). Although radiative transfer calculations for a disk+corona configuration (rather than those for a bare disk above) result in a weaker "UV turnover" (Kawaguchi et al. 2001), the expected spectra are redder than the long wavelength limit of the standard disk as well. In addition, the accretion disk of quasars or luminous AGNs is thought to be seen almost face-on, so the relativistic effects for the color of the observed spectrum is probably negligible (Hubeny et al. 2000). In short, it is difficult to explain the flux difference spectrum with $\alpha_\nu^{\rm dif} \sim 1/3$ by any of the existing accretion disk models.

However, it is true that the reasonable range of physical parameters related to the accretion disk model ($M_{\rm BH}$ and Eddington ratio) can qualitatively explain the absolute continuum flux and flux variation amplitude as indicated in Sakata et al. (2011) and Gu & Li (2013), and $\alpha_\nu^{\rm dif}$ obtained here can be naturally attributed to the well-known long wavelength limit value predicted in standard accretion disk models. Thus, we can only conclude that the continuum spectral variability in quasars cannot be explained by the accretion disk model with varying mass accretion rate, but it is probably related to thermal accretion disk itself. Finally, we note that it seems to be difficult to explain the large coherent flux variation within UV–optical wavelength range (e.g., a strong linear flux–flux correlation in each individual quasar) by the accretion disk local fluctuations or hot spot scenarios (e.g., Dexter & Agol 2011; Schmidt et al. 2012; Meusinger & Weiss 2013).

### 4.4. *Brief Summary of This Section*

In summary, our conclusions in this section are:

1. We show that the continuum component of the flux difference spectra is (in average) well approximated by a power-law shape with $\alpha_\nu^{\rm dif} \sim +1/3$, and it is bluer than the spectroscopic composite flux difference spectrum ($\alpha_\nu^{\rm dif} = 0.0$) obtained by Wilhite et al. (2005). We conclude that the discrepancy is due to the Galactic extinction; the light curves used in our analyses are corrected for Galactic extinction but the spectra used in Wilhite et al. (2005) are not. If we derive the color of the flux difference spectrum without the correction, our result shows consistent color and rest-frame wavelength dependence of the flux difference spectrum with Wilhite et al. (2005), in spite of the large difference in time scale (Figure 4).

2. We compare the $b(s,l)$–redshift relation with "the standard disk with varying mass accretion rate model" (Pereyra et al. 2006). One of the advantages of our method is that it is based on the direct comparison of observable color of the difference spectrum ($b(s,l)$) with the model predicted difference spectrum, and does not require additional models or assumptions for non-variable spectral components. We concluded that the flux difference spectrum is flatter (bluer) than the model prediction. In particular, we confirm that the model-predicted "UV turnover" is not seen in the flux difference spectrum. This is surprising because not only the standard accretion disk model (Shakura & Sunyaev 1973) but also any accretion disk models cannot produce such a flat spectrum as $\alpha_\nu^{\rm dif} \sim +1/3$. This result is qualitatively consistent with Schmidt et al. (2012), but our method enables us to examine the difference between observed variability and the model prediction quantitatively.

## 5. EMISSION LINE VARIABILITY: THE ORIGIN OF THE REDSHIFT DEPENDENCE OF THE COLOR OF THE FLUX DIFFERENCE SPECTRUM

The flux difference spectra are composed of the continuum component (accretion disk emission) and the BELs component. The regression slope $b(s,l)$ can be related to the difference spectrum as in Equation (4), and as we have seen in Section 3.3 (Figure 5), emission line variability on the power-law continuum variability makes bumpy features in $b(s,l)$–redshift space. Many of the features in the color-redshift (i.e., $b^{\rm ratio}(s,l)$–redshift, or $b(s,l)$–redshift) relations are caused by more than one feature in the quasar spectrum (Richards et al. 2001). We are able to infer the contribution of each of the emission line variability to the flux difference spectrum by examining the $b(s,l)$–redshift relation.

We show the effects of the variability of each of the prominent BEL on $b(r,i)$ and $b(g,i)$ as a function of redshift in Figures 12 and 13, respectively. "Emission lines" contain BELs, Balmer and Paschen continuum emission (BaC and PaC), and Fe II pseudo-continuum emission. They are calculated assuming

$$f_\lambda^{\rm dif} = f_\lambda^{\rm dif}({\rm continuum}) + 0.05 \times f_\lambda^{\rm dif}({\rm line}) \qquad (19)$$

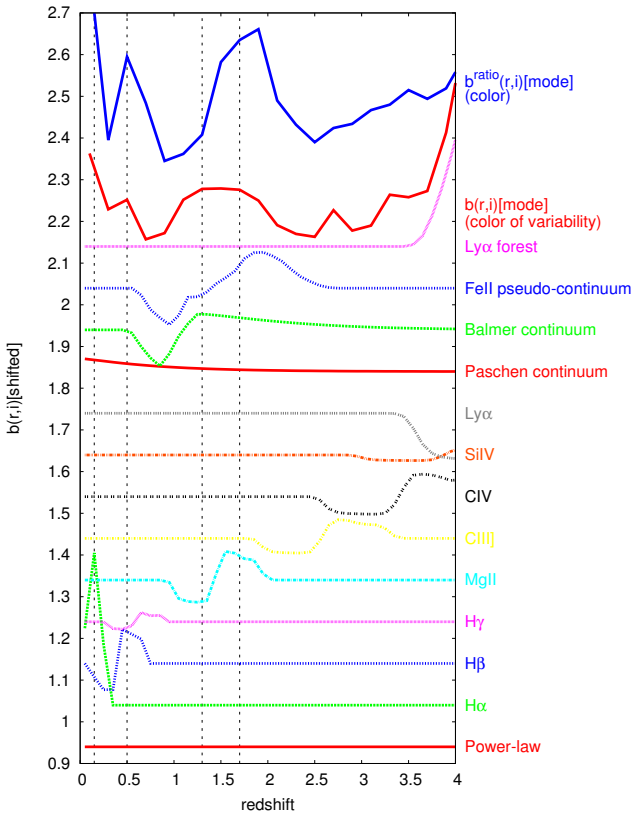


FIG. 12.— $b(r,i)$ as a function of redshift. Each curve (except for the top two curves) is calculated by Equation (4) assuming a difference spectrum $f_\nu^{\rm dif}$ composed of power-law continuum and one additional spectral component: the broad emission lines, Balmer and Paschen continuum, or Ly$\alpha$ forests (Equations (19) and (20)). The solid curve labeled "$b^{\rm ratio}(r,i)$[mode]" (colored blue in the electronic edition) is the modal color of the time-averaged spectrum $b^{\rm ratio}(r,i)$ as a function of redshift. The solid curve labeled "$b(r,i)$[mode]" (colored red in the electronic edition) is the modal color of the difference spectrum ($b(r,i)$) as a function of redshift. Curves (other than the "power-law" model) are shifted vertically, and the offset is taken to be 0.1 from adjacent curves.

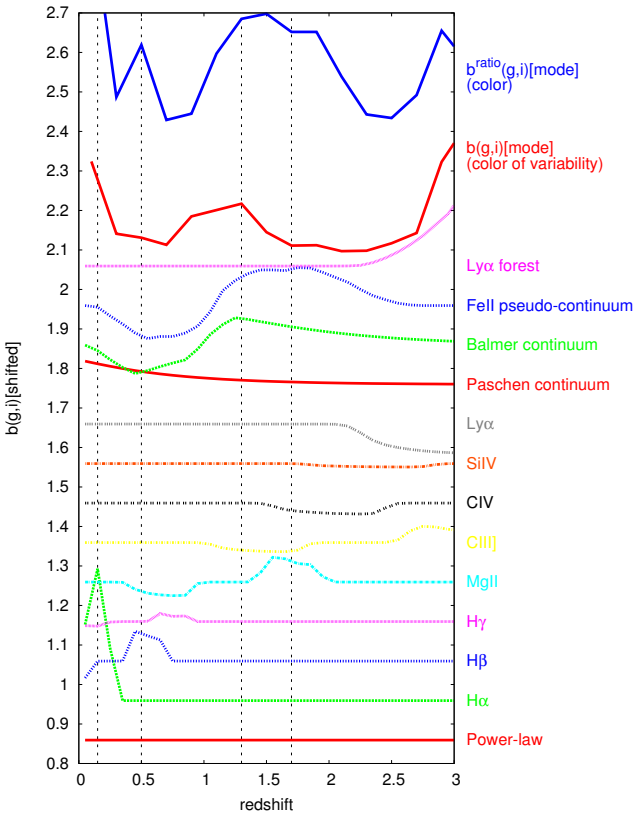


FIG. 13.— Same as Figure 12, but for $b(g,i)$ and $b^{\rm ratio}(g,i)$.

where $f_\lambda^{\rm dif}$(continuum) is the power-law continuum variable component (Equation (16)) normalized to 1 at 3000Å , and given as

$$f_\lambda^{\rm dif}({\rm continuum}) = \left(\frac{\lambda}{3000{\rm Å}}\right)^{-7/3} \qquad (20)$$

$f_\lambda^{\rm dif}$(line) includes $f_\lambda^{\rm dif}$(BEL), $f_\lambda^{\rm dif}$(BaC), $f_\lambda^{\rm dif}$(PaC), and $f_\lambda^{\rm dif}$(Fe II). The factor "0.05" in Equation (19) is an overall normalization constant for emission line components to a power-law continuum component and is determined to approximately reproduce the amplitude of bumpy features in the observed $b(s,l)$–redshift relation. The analytical expressions for calculating these components, and the IGM attenuation model (labeled "Ly$\alpha$ forest") are summarized in Appendix A. In Figures 12 and 13, the relative strengths of these components are taken into consideration as described in Appendix A.

Here, we discuss several features of $b^{\rm ratio}(r,i)$–redshift relation and $b(r,i)$–redshift relation qualitatively. We focus on the case of $(r,i)$ band pair, but the color–redshift relation of other band pairs can be interpreted in the same way.

By comparing $b(r,i)$–redshift relation with $b^{\rm ratio}(r,i)$–redshift relation in Figure 12, we are able to identify several similarities and differences in the features. Features of Balmer emission lines and Balmer continuum are seen in both $b(r,i)$ and $b^{\rm ratio}(r,i)$. The most significant difference between $b(r,i)$ and $b^{\rm ratio}(r,i)$ exists in features of the Fe II pseudo-continuum and the Mg II emission line. As was done in Richards et al. (2001), we can identify each of the significant features in the $b^{\rm ratio}(r,i)$-redshift relation and $b(r,i)$–redshift relation for each redshift range as below:

- $z \sim 0.1$ to 0.2 — H$\alpha$ is in $i$-band and makes $b^{\rm ratio}(r,i)$ and $b(r,i)$ redder than the average power-law value. Also, the Paschen continuum emission possibly makes the color slightly redder (e.g., Landt et al. 2011).
- $z \sim 0.3$ — The presence of H$\beta$ in $r$-band drives $b^{\rm ratio}(r,i)$ and $b(r,i)$ blueward.
- $z \sim 0.5$ — $b^{\rm ratio}(r,i)$ and $b(r,i)$ moves back to red color while H$\beta$ is in $i$-band.
- $z \sim 0.7$ — Balmer continuum enters the $r$-band making $b^{\rm ratio}(r,i)$ and $b(r,i)$ bluer.
- $z \sim 0.9$ — Fe II and Mg II fill the $r$-band making $b^{\rm ratio}(r,i)$ bluer. However, these features seem to be absent in $b(r,i)$.
- $z \sim 1.4$ to 1.5 — $b^{\rm ratio}(r,i)$ makes a sharp transition from blue to red as Mg II leaves $r$-band and enters $i$-band. This transition seems to be absent in $b(r,i)$
- $z \sim 1.8$ — A small hump is caused as both Mg II and Fe II push $b^{\rm ratio}(r,i)$ redward. Again, this feature is absent in $b(r,i)$.

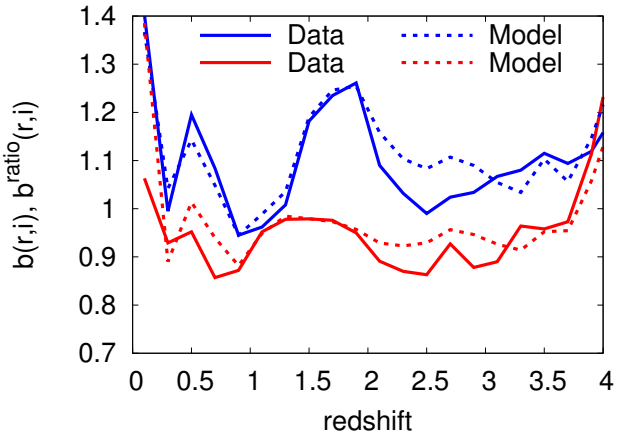


FIG. 14.— Comparison of observed $b^{\rm ratio}(r,i)$ (upper solid line, colored blue in the electronic edition) and $b(r,i)$ (lower solid line, colored red in the electronic edition) with those of model spectra (dotted lines) as a function of redshift . The model spectra are the sum of a power-law component ($\alpha_\lambda = -1.56$ and $\alpha_\lambda^{\rm dif} = -7/3$ for $b^{\rm ratio}(r,i)$ and $b(r,i)$, respectively) (scaled to 1 at 3000Å, as Equation (20)), and several additional components as below: In the model spectrum for $b^{\rm ratio}(r,i)$ (upper dotted line, colored blue in the electronic edition), all the emission line components shown in Figure 12, Balmer and Paschen continuum emission, and Fe II pseudo-continuum emission are included and the IGM attenuation is applied (the relative strengths of each of the components are the same as Appendix A). On the other hand, in the model spectrum for $b(r,i)$ (lower dotted line, colored red in the electronic edition) we exclude Mg II emission line and Fe II pseudo-continuum emission. Note that there exist many kinds of weaker high-ionization lines between C III] and C IV that we do not show in Figure 12/13 (e.g.,Fe III, Al III, N III], and N IV), so the model spectra have redder color than the observed color both in $b^{\rm ratio}(r,i)$ and $b(r,i)$.

- $z \sim 2.0$ to 2.5 — $b^{\rm ratio}(r,i)$ is driven back to the blue as Fe II leaves $i$-band. $b(r,i)$ also becomes blue, probably because of the contribution from C III] in $b(r,i)$. Note that there exist many kinds of weaker high-ionization lines between C III] and C IV that we do not show (e.g.,Fe III, Al III, N III], and N IV), and they also make $b^{\rm ratio}(r,i)$ and $b(r,i)$ bluer.

- $z \sim 2.6$ to 3.4 — C IV and C III] offset each other when the former is in $r$-band and the latter is in $i$-band, and keeps $b^{\rm ratio}(r,i)$ and $b(r,i)$ blue.

- $z > 3.4$ — Ly$\alpha$ and C IV offset each other during the period when the former is in $r$-band and the latter is in $i$-band. At higher redshift, $b^{\rm ratio}(r,i)$ and $b(r,i)$ rises rapidly as the Ly$\alpha$ forest or Lyman-limit systems absorb $r$-band flux (see Figure 16).

In Figure 14, we show the comparison of the observed $b^{\rm ratio}(r,i)$ (upper solid curve) and $b(r,i)$ (lower solid curve) with those of model spectra(dotted curves) as a function of redshift. The model spectra are the sum of a power-law component ($\alpha_\nu = -1.56$ and $\alpha_\nu^{\rm dif} = -7/3$ for $b^{\rm ratio}(r,i)$ and $b(r,i)$, respectively (scaled to 1 at 3000Å, as Equation (20)), and several additional components as below: In the model spectrum for $b^{\rm ratio}(r,i)$ (upper dotted curve), all the emission line components shown in Figure 12, Balmer and Paschen continuum emission, and Fe II pseudo-continuum emission are included, and the IGM attenuation is applied (the relative strengths of each of the components are the same as Appendix A). On the other hand, in the model spectrum for $b(r,i)$ (lower dotted curve) we exclude Mg II emission line and Fe II pseudo-continuum emission. Note that there exist many kinds of weaker high-ionization lines between C III] and C IV that we do not show in Figure 12/13 (e.g.,Fe III, Al III, N III], and N IV), so the model spectra have redder color than the observed color both in $b^{\rm ratio}(r,i)$ and $b(r,i)$. Nevertheless, it is clear that the model spectra successfully reproduce the observed bumpy feature in $b(s,l)$–redshift and $b^{\rm ratio}(s,l)$–redshift relations. Moreover, it is also clearly shown that the differences between $b^{\rm ratio}(s,l)$ and $b(s,l)$ as a function of redshift exist not only in the continuum power-law spectral index, but also in the relative significance of the emission line components; Mg II and Fe II emission line components seem not to play an important role in the $b(s,l)$–redshift relation, although they have significant contribution in the $b^{\rm ratio}(r,i)$–redshift relation.

In summary:

1. Utilizing the average $b^{\rm ratio}(s,l)$–redshift relation, we can identify the emission line contamination in the color of the quasars (Richards et al. 2001) as bumpy features in $b^{\rm ratio}(s,l)$–redshift curves. Applying this method to the $b(s,l)$–redshift relation, we identify the features due to, for instance, Balmer emission lines and Balmer continuum variability in $b(s,l)$–redshift relation.

2. We show that several features seen in $b^{\rm ratio}(s,l)$–redshift and $b(s,l)$–redshift relation are similar (e.g., the Balmer series emission), but they look significantly different around the features attributable to the broad Mg II emission line. This indicates that the variability of Mg II emission line and Fe II pseudo-continuum emission seem to be relatively weaker than other emission line components, such as Balmer series emission lines. This spectral region (referred to as "SBB") also contains the Balmer continuum, Fe II pseudo-continuum emission, and some other (relatively weak) high-ionization lines, so detailed spectral decomposition analysis is needed to infer the variability of each component, and this is attempted in the next section.

## 6. VARIABILITY OF THE SMALL BLUE BUMP

In this section, we focus on the variability of the SBB spectral components. First we decompose the high resolution composite spectrum of Vanden Berk et al. (2001) into spectral components, and compose several model spectra by combining some of the components. Then, we calculate the $b(r,i)$–redshift relation of each of the model spectrum and compare it with the observed $b(r,i)$–redshift relation. This procedure enables us to identify the (non-)variable spectral components in the SBB.

### 6.1. *Spectral Decomposition*

As seen in Figure 7 and discussed in the previous section, the most apparent difference between $b^{\rm ratio}(s,l)$[color of the time-averaged spectrum] and $b(s,l)$[color of the flux difference spectrum] exists in features of the Fe II pseudo-continuum and the Mg II emission line. The spectral region containing Fe II pseudo-continuum, Balmer continuum emission, and Mg II emission line is called SBB (Wills et al. 1985). Note that in the actual quasar spectra, higher order Balmer lines are merging to a pseudo-continuum and yielding a smooth rise to the Balmer edge (Dietrich et al. 2003), which is also contained in SBB. Here we discuss the SBB variability.

To clarify the difference between $b^{\rm ratio}(s,l)$ and $b(s,l)$ (as a function of redshift) arising from the complex emission line

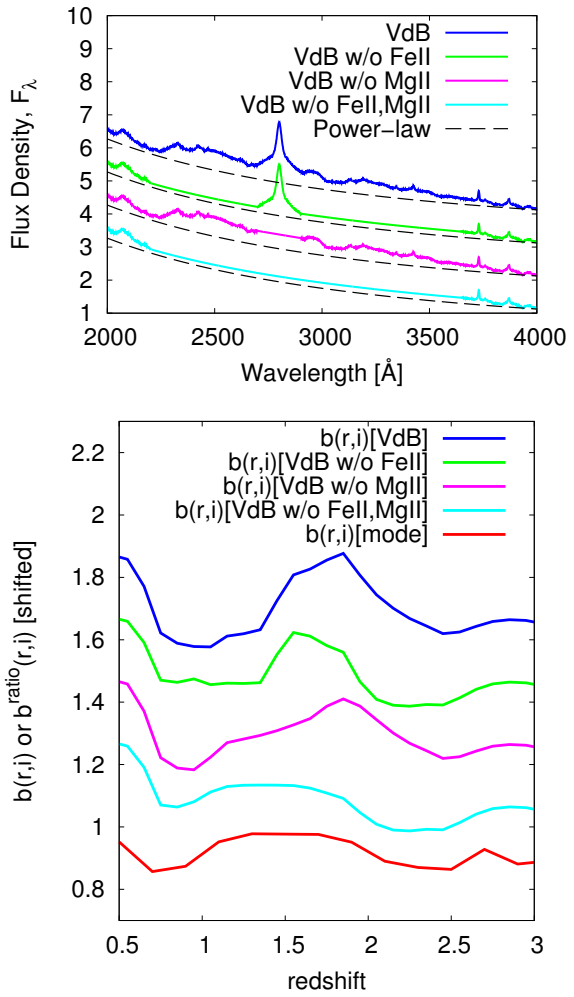


FIG. 15.— Upper panel: decomposition of the Small Blue Bump (2200Å - 3646Å) in the composite spectrum (Vanden Berk et al. 2001) following Kurk et al. (2007). "VdB" indicate the Vanden Berk's quasar composite spectrum. From top to bottom, solid curves indicate the raw composite spectrum (VdB), the Fe II-subtracted composite spectrum (VdB w/o Fe II), the Mg II-subtracted composite spectrum (VdB w/o Mg II), and the Fe II-Mg II-subtracted composite spectrum (VdB w/o Fe II, Mg II), respectively (colored blue, green, magenta, and cyan in the electronic edition). These spectra are shifted by +3.0, 2.0, 1.0, and 0.0 in *y*-axis, respectively. The continuum power-law index is $\alpha_\lambda = -1.54$ and the power-law component is normalized to the flux values in the 4200-4230Å region (dashed lines). The Balmer continuum is created by Equation (A2) and normalized to the value at 3675Å. Mg II is decomposed by linearly interpolating the spectrum through 2700Å to 2900Å. Bottom panel: the color of the redshifted spectra in upper panel as a function of redshift (upper four curves), compared with the observed modal color of the difference spectrum ($b(r,i)$) as a function of redshift (bottom solid curve, the same as Figure 7). From top to bottom, the upper four curves are shifted by +0.6, 0.4, 0.2 and 0.0 in the *y*-axis, respectively (colored blue, green, magenta, and cyan, respectively, in the electronic edition). The composite spectrum without Fe II pseudo-continuum and the Mg II emission line (VdB w/o Fe II,Mg II), which means this spectrum is composed of a power-law continuum and the Balmer continuum emission, has a similar color–redshift relation with the observed $b(r,i)$–redshift curve. Note that the host galaxy contamination in the VdB composite spectrum is not subtracted.

composition, we decompose the SBB in the composite spectrum (Vanden Berk et al. 2001) into power-law continuum, Mg II emission line, Fe II pseudo-continuum, and Balmer continuum and investigate the color (corresponding to $b^{\rm ratio}(s,l)$ and $b(s,l)$) as a function of redshift for the composite spectra with and without some SBB components.

Kurk et al. (2007) decomposed the Vanden Berk's composite spectrum into a power-law continuum, Balmer continuum, and residual. They confirmed that the residual was well described by the Fe II emission template (Vestergaard & Wilkes 2001) and a Mg II emission line. We follow their decomposition procedure, which is done in the 2200-3646Å region. First, the power-law continuum with $\alpha_\lambda = -1.54$ is normalized to the values in the 4200-4230Å region. Second, the Balmer continuum is created by Equation (A2) and normalized to the value at 3675Å . The residual spectrum (the composite spectrum minus a power-law minus Balmer continuum) is composed of Fe II pseudo-continuum and a Mg II emission line. The Mg II emission line is decomposed by simply assuming the Fe II pseudo-continuum in 2700Å to 2900Å region is described by linear interpolation of the residual spectrum from 2700Å to 2900Å.

Using the decomposed components, we define four spectra of the SBB region $f_\lambda$(SBB) as below:

- VdB: the composite spectrum of Vanden Berk et al. (2001).

$$f_\lambda({\rm SBB}) = f_\lambda({\rm PL}) + f_\lambda({\rm BaC}) + f_\lambda({\rm Fe\ II}) + f_\lambda({\rm Mg\ II}) \quad (21)$$

  where "PL" denotes a power-law component.

- VdB w/o Fe II: VdB minus Fe II pseudo-continuum.

$$f_\lambda({\rm SBB}) = f_\lambda({\rm PL}) + f_\lambda({\rm BaC}) + f_\lambda({\rm Mg\ II}). \quad (22)$$

- VdB w/o Mg II: VdB minus Mg II emission line

$$f_\lambda({\rm SBB}) = f_\lambda({\rm PL}) + f_\lambda({\rm BaC}) + f_\lambda({\rm Fe\ II}). \quad (23)$$

- VdB w/o Fe II , Mg II: VdB minus Fe II pseudo-continuum minus Mg II emission line

$$f_\lambda({\rm SBB}) = f_\lambda({\rm PL}) + f_\lambda({\rm BaC}). \quad (24)$$

These spectra are shown in the upper panel of Figure 15. Then, we calculate the color of these spectra by Equation (4) or (10) as a function of redshift. Results are shown in the bottom panel of Figure 15. We can see that the Balmer continuum, Fe II pseudo-continuum, and the Mg II emission line make distinguishable bump features at different redshift ranges. The peak in $b(r,i)$[VdB] at $z \sim 1.5$-1.8 are made of a Mg II emission line ($z \sim 1.5$) and Fe II pseudo-continuum ($z \sim 1.8$) (in agreement with Richards et al. 2001), and this feature is not seen in the $b(r,i)$[mode]. The $b(r,i)$[mode] curve resembles the case of "VdB w/o Fe II, Mg II" (i.e., $f_\lambda({\rm SBB}) = f_\lambda({\rm PL}) + f_\lambda({\rm BaC})$. This indicates that the variability of Mg II emission line and Fe II pseudo-continuum are relatively weaker compared to the Balmer continuum emission.

### 6.2. *Mg II Emission Line Variability*

Mg II line variability has been examined in several papers (see Woo 2008; Hryniewicz et al. 2013, and references therein). Goad et al. (1999a,b) showed that continuum flux and the broad high-ionization emission lines of Ly$\alpha$, C IV, N V(1240Å), He II(1640Å), and the semi-forbidden lines of the Si III]+C III] blend varied significantly (a factor of 5 at 1365Å and 3 at 2230Å for continuum, and a factor of 2 for Ly$\alpha$ and C IV), while the low-ionization lines of Mg II and Fe II do not vary significantly (less than 7%) during 11 months of observations for the Seyfert 1 galaxy NGC 3516. Goad et al. (1999a) listed three possible physical reasons explaining an absence of response in the Mg II emission line: (1)

the continuum band responsible for the Mg II emission line (i.e., 600 to 800 eV, Krolik & Kallman 1988) is invariant; (2) the emission line is insensitive to continuum variations; and (3) the line-emitting region is physically extended and thus has yet to respond to the observed continuum variations. (1) was denied in Goad et al. (1999a) by observational evidence that showed that the amplitude of the continuum variations generally increase toward shorter wavelengths at least up to EUV wavelength range for several AGNs (e.g., Marshall et al. 1997; Cagnoni et al. 1999; Halpern et al. 2003). Strong soft X-ray variability has been observed in many AGNs, so (1) is definitely not true. (3) is not true, especially in our sample, with three to four years (in quasar rest-frame) observational duration. Thus, we are able to expect situation (2) to be responsible for an absence of variability in the Mg II emission line. Goad et al. (1993) defined the line responsivity $\eta$ as a linear coefficient relating line emissivity with ionization parameter, assuming that locally the emission-line gas responds linearly to continuum variations (Goad et al. 1999a; Korista & Goad 2004; Goad et al. 2012). The larger $\eta$ is, the more responsive the line is to continuum variations. Although $\eta$ is model dependent, high-ionization emission lines generally have $\eta \sim 1$; Balmer lines have $\eta \sim 0.6$; and Mg II emission line has $\eta \sim 0.2$ (Goad et al. 1999a; Korista & Goad 2004). We are able to interpret our result with respect to the weak variability of Mg II as the consequence of the small responsivity $\eta$ for the low-ionization lines.

### 6.3. *Fe II Pseudo-continuum Variability*

The Fe II emission line is also a member of the low-ionization lines. In the same way as the Mg II emission line, the weak variability of Fe II can be the consequence of the small responsivity $\eta$. However, the situation may be more complicated in regards to the Fe II.

The origin of Fe II emissions is still controversial (e.g., Dong et al. 2011). Baldwin et al. (2004) showed that Fe II emissions from photoionized broad emission line region (BELR) cannot explain all the Fe II emission features, and suggested that a large amount of Fe II emission originates in either a separate collisionally ionized component or BELR with considerable velocity structure (microturbulence). The collisionally ionized component would not vary in response to continuum variations, thus Fe II pseudo-continuum variability would be weak as a whole. On the other hand, several authors suggest that Fe II is emitted in infalling photoionized gas (Hu et al. 2008; Ferland et al. 2009), and several recent observational evidences support this picture (Barth et al. 2013, and references therein). When this is the case, the small amplitude of Fe II variability can be explained as the consequence of the different origin of Fe II, (i.e., Fe II emission does not come from usual BELR, so it cannot vary in the same way as other BELs). However, more detailed investigation of the Fe II emission is beyond the scope of this paper.

### 6.4. *Balmer Continuum Variability*

Figure 15 indicates that the Balmer continuum is a dominant variable component in SBB region. We can expect that the Balmer continuum and Balmer emission lines are formed coherently by some photoionization processes in the broad line region, as we can see in the fourth global eigenspectrum presented by Yip et al. (2004). There is no wonder that the Balmer continuum is variable like the Balmer emission lines (e.g., H$\alpha$ and H$\beta$). The variability of the Balmer continuum has been discussed observationally in Wamsteker et al. (1990) and Maoz et al. (1993), and theoretically in Korista & Goad (2001). Our result is the first study clearly showing the variability of the Balmer continuum emission in large quasar samples.

Wilhite et al. (2005) showed that the ratio spectrum of the composite difference spectrum to the composite spectrum was depressed around 3000Å (see also Bian et al. 2012). Photometric variability using structure function formalization (Vanden Berk et al. 2004; MacLeod et al. 2012) also shows the depression around 3000Å. This behavior can be interpreted by our result about the variability and non-variability of SBB components. Because the Fe II pseudo-continuum ($\sim$ 2200-3000Å) and Mg II emission line ($\sim$ 2800Å) exist in the composite spectrum although not in the composite difference spectrum, the ratio is significantly depressed. Moreover, as discussed in Bian et al. (2012), the Balmer continuum should obey the intrinsic Baldwin effect in the same way as Balmer emission lines, so the ratio spectrum around the Balmer continuum region should be slightly depressed.

### 6.5. *Brief Summary of This Section*

In summary, our conclusions in this section are:

1. We first decompose the SBB spectral region of the high resolution SDSS quasar composite spectrum (Vanden Berk et al. 2001) into a power-law continuum, Balmer continuum, Fe II, and Mg II following Kurk et al. (2007). Then, we investigate the color–redshift relation of the composite spectrum with and without each component. We confirm that the composite spectrum without Fe II and Mg II emission line components has similar color–redshift relations with the color of the flux difference spectrum. This indicates that Fe II and Mg II have (in average) small variability, and the Balmer continuum is variable in broad spectral region. This is the first time that the strong variability of Balmer continuum and small variability of Fe II and Mg II are confirmed as the statistical property of large quasar samples.

2. Small variability of the Mg II emission line is naturally interpreted by the small responsivity $\eta$ of the low-ionization line to the ionizing continuum variation (Goad et al. 1999a).

3. Small variability of the Fe II emission line is also interpreted by the small responsivity $\eta$ of the low-ionization line, but the origin of the Fe II emission is controversial, so it is possible that the small variability of Fe II is due to the different origin of Fe II from normal photoionization BELR.

4. It is no wonder that the Balmer continuum is variable like the other Balmer emission lines because we can expect that they are formed coherently by some photoionization processes in the broad line region.

## 7. CONCLUSIONS

We have explored the wavelength dependence of quasar long term variability. We have introduced the flux–flux correlation method, and applied it to a database of SDSS Stripe 82 multi-epoch five-band light curves for spectroscopically confirmed quasars. This method enables us to infer the spectral variability without suffering from time-averaged baseline

flux, which includes time-constant quasar host galaxy flux contamination and time-averaged emission line flux contaminations.

In this paper, we focused on the statistical properties of the quasar UV−optical variability, and we conclude:

1. In Section 4, we show that the continuum component of the flux difference spectra is (on average) well approximated by a power-law shape with $\alpha_\nu^{\rm dif} \sim +1/3$. Then, we compare the $b(s,l)$–redshift relation with "the standard disk with varying mass accretion rate model" (Pereyra et al. 2006). We concluded that the flux difference spectrum is flatter (bluer) than the model prediction. In particular, we confirm that the model-predicted "UV turnover" is not seen in the flux difference spectrum. This is surprising because not only the standard accretion disk model (Shakura & Sunyaev 1973) but also any accretion disk models cannot produce such a flat spectrum as $\alpha_\nu^{\rm dif} \sim +1/3$. We stress the importance of the correction for Galactic extinction, without which the flux difference spectrum happens to have similar spectral shape with the model spectrum.

2. In Section 5, we identify the features due to, for instance, Balmer emission lines and Balmer continuum variability in the $b(s,l)$–redshift relation. We show that some of the features seen in $b^{\rm ratio}(s,l)$–redshift and $b(s,l)$–redshift relation are similar (e.g., the Balmer series emission), but they look significantly different around the SBB spectral region. It indicates that the variability of Mg II emission lines and Fe II pseudo-continuum emission seem to be relatively weaker than other emission line components, such as the Balmer series emission lines.

3. In Section 6, we first decompose the SBB spectral region of the high resolution SDSS quasar composite spectrum (Vanden Berk et al. 2001) into a power-law continuum, Balmer continuum, Fe II, and Mg II following Kurk et al. (2007). Then, we investigate the color−redshift relation of the composite spectrum with and without each component. We confirm that the composite spectrum without Fe II and Mg II emission line components has similar color−redshift relations with the color of the flux difference spectrum. This indicates that Fe II and Mg II have (in average) small variability, and the Balmer continuum is variable in broad spectral region. This is the first time that the strong variability of the Balmer continuum and the small variability of Fe II and Mg II are confirmed as the statistical property of large quasar samples. The small variability of the Mg II emission lines and Fe II emission lines is naturally interpreted by the small responsivity $\eta$ of the low-ionization line to the ionizing continuum variation (Goad et al. 1999a). However, the origin of the Fe II emission is controversial, so it is possible that the small variability of Fe II is due to the different origin of Fe II from normal photoionization BELR. It is no wonder that the Balmer continuum is variable like the other Balmer emission lines, as we can expect that they are formed coherently by some photoionization processes in the broad line region.

In the present work, we have limited our discussion to the UV−optical variability and UV−optical data. However, it is clear that the AGN variability should be understood as multi-wavelength phenomena. The correlation between the X-ray and UV−optical variability is definitely important. The X-ray reprocessing model, which also predicts the bluer-when-brighter UV−optical color variability with $\alpha_\nu^{\rm dif} \sim +1/3$ if simple geometry for the X-ray emitting region and the accretion disk is assumed, may be the alternative model for AGN UV−optical variability ("the lamp-post model"; e.g., Tomita et al. 2006; Cackett et al. 2007; Lira et al. 2011; Gil-Merino et al. 2012; Chelouche 2013). This model also explains the variability time-scale (nearly simultaneous UV-to-optical variability) as the light-crossing time of the accretion disk. However, the geometry around the accretion disk and the X-ray emitting region is not well known, and definitive conclusions about the validity of the X-ray reprocessing model have not been obtained yet. The correlation between UV−optical and X-ray variability has been observed in several AGNs (e.g., Breedt et al. 2009; Cameron et al. 2012), but sometimes conflicting results with the X-ray reprocessing model have been obtained (e.g., Maoz et al. 2002; Shemmer et al. 2003; Marshall et al. 2008). Future multi-wavelength intensive monitoring for more AGNs will be needed to clarify the origin of the X-ray−UV−optical correlation.

The present work deals with the properties of spectral variability only in the composite sense. In a second paper, we would discuss the dependence of the spectral variability on several physical parameters, and (in)validity of the physical models for continuum variability in more detail.

We thank Makoto Kishimoto for useful discussions and comments. This work is supported by Grants-in-Aid for Scientific Research (22540247, 25287062). Data analysis were in part carried out on common use data analysis computer system (pc08, IDL8.1) at the Astronomy Data Center, ADC, of the National Astronomical Observatory of Japan.

Funding for the SDSS and SDSS-II has been provided by the Alfred P. Sloan Foundation, the Participating Institutions, the National Science Foundation, the U.S. Department of Energy, the National Aeronautics and Space Administration, the Japanese Monbukagakusho, the Max Planck Society, and the Higher Education Funding Council for England. The SDSS website is http://www.sdss.org/.

The SDSS is managed by the Astrophysical Research Consortium for the Participating Institutions, which are the American Museum of Natural History, Astrophysical Institute Potsdam, University of Basel, University of Cambridge, Case Western Reserve University, University of Chicago, Drexel University, Fermilab, the Institute for Advanced Study, the Japan Participation Group, Johns Hopkins University, the Joint Institute for Nuclear Astrophysics, the Kavli Institute for Particle Astrophysics and Cosmology, the Korean Scientist Group, the Chinese Academy of Sciences (LAMOST), Los Alamos National Laboratory, the Max-Planck-Institute for Astronomy (MPIA), the Max-Planck-Institute for Astrophysics (MPA), New Mexico State University, Ohio State University, University of Pittsburgh, University of Portsmouth, Princeton University, the United States Naval

TABLE 2
THE COMPOSITE SPECTRAL PROPERTY OF BROAD EMISSION LINES

| Line | $\lambda_{\rm rest}$[Å] | $R$(Rel.Flux[100× $F/F$(Ly$\alpha$)]) | $\sigma_\lambda$[Å] |
|---|---|---|---|
| H$\alpha$ | 6564.61 | 30.832 | 47.39 |
| H$\beta$ | 4862.68 | 8.649 | 40.44 |
| H$\gamma$ | 4341.68 | 2.616 | 20.32 |
| Mg II | 2798.75 | 14.725 | 34.95 |
| C III] | 1908.73 | 15.943 | 23.58 |
| C IV | 1549.06 | 25.291 | 14.33 |
| Si IV | 1396.76 | 8.916 | 12.50 |
| Ly$\alpha$ | 1215.67 | 100.000 | 19.46 |

REFERENCES. — Vanden Berk et al. (2001).

Observatory, and the University of Washington.

## APPENDIX

## A: MODEL SPECTRA USED IN SECTION 5

Here we show how model spectra in Section 5 are calculated.

**Broad emission lines:** $f_\nu^{\rm dif}$(BEL) include H$\alpha$, H$\beta$, H$\gamma$, Mg II, C III],C IV, Si IV, Ly$\alpha$, which are the eight strongest BELs in the SDSS quasar composite spectrum (Vanden Berk et al. 2001), and calculated as

$$f_\lambda^{\rm dif}({\rm BEL}) = R\frac{\sigma_\lambda({\rm Ly}\alpha)}{\sigma_\lambda}\exp\left(-\left(\frac{(\lambda-\lambda_{\rm rest})^2}{2\sigma_\lambda^2}\right)\right) \quad ({\rm A1})$$

where $\lambda_{\rm rest}$ (rest-frame central wavelength for an emission line), $R$ (relative strength for each BEL), and $\sigma_\lambda$ (line width) are given as Table 2 for each emission line (Vanden Berk et al. 2001).

**Balmer and Paschen continuum emission:** For $f_\lambda^{\rm dif}$(BaC) and $f_\lambda^{\rm dif}$(PaC), we assume gas clouds of uniform temperature ($T_e$=15000 K) that are partially optically thick (Dietrich et al. 2003; Kurk et al. 2007). We assume that the Balmer continuum spectrum variability below the Balmer edge $\lambda_{\rm BE}$ = 3646Å is described by

$$f_\lambda^{\rm dif}({\rm BaC}) = R^{\rm BaC}B_\lambda(T_e)\left(1-\exp\left(-\tau_{\rm BE}\left(\frac{\lambda}{\lambda_{\rm BE}}\right)^3\right)\right) \quad ({\rm A2})$$

where $B_\lambda(T_e)$ is the Planck function at the electron temperature $T_e$, $\tau_{\rm BE}$ is the optical depth at the Balmer edge $\lambda_{\rm BE}$ = 3646Å , and $R^{\rm BaC}$ is the normalized flux density at the Balmer edge (Grandi 1982). The optical depth is fixed at $\tau_{\rm BE}$ = 1 (Kurk et al. 2007) and $R^{\rm BaC}$ (with relative strength to other emission lines) is determined by the integrated flux ratio $F^{\rm BaC}/F$(H$\alpha$) = 1.80 (Grandi 1982). Note that in the actual quasar spectra, higher order Balmer lines are merging to a pseudo-continuum, yielding a smooth rise to the Balmer edge (Wills et al. 1985; Dietrich et al. 2003). In the same way as the Balmer continuum, the Paschen continuum variability is expressed by

$$f_\lambda^{\rm dif}({\rm PaC}) = R^{\rm PaC}B_\lambda(T_e)\left(1-\exp\left(-\tau_{\rm PE}\left(\frac{\lambda}{\lambda_{\rm PE}}\right)^3\right)\right) \quad ({\rm A3})$$

where $\lambda_{\rm PE}$ = 8208Å the optical depth is fixed at $\tau_{\rm PE}$ = 0.25, and $R^{\rm PaC}$ is determined by the integrated flux ratio $F^{\rm PaC}/F$(H$\alpha$) = 1.17 (Grandi 1982).

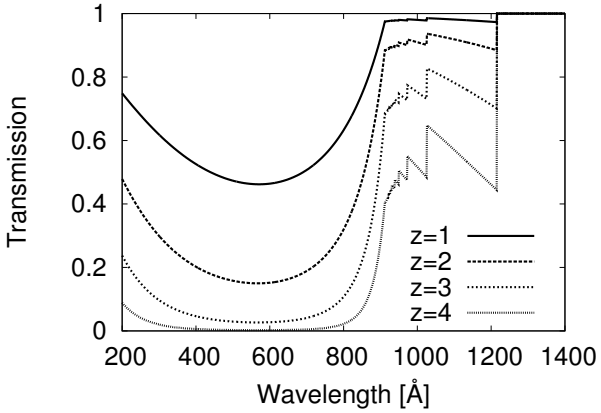


FIG. 16.— Transmissivity exp($-\tau_{\rm eff}(z,\lambda)$) as a function of rest-frame wavelength, where $\tau_{\rm eff}$ is the effective optical depth of the IGM (Meiksin 2006).

**Fe II pseudo-continuum emission:** The "SBB" is composed not only of the Balmer continuum and Mg II BEL, but also of Fe II pseudo-continuum emission. To model the Fe II pseudo-continuum emission, we adopt a UV Fe II emission template presented by Tsuzuki et al. (2006). As we do not know the relative strength of Fe II emission to the power-law continuum or the other components in the SBB, we choose to scale the peak value of the Fe II template at $\lambda$ = 2481.9299Å to have $f_\lambda$ = 0.3, then

$$f_\lambda^{\rm dif}({\rm Fe\ II}) = f_\lambda({\rm Fe\ II\ template,\ scaled}). \quad ({\rm A4})$$

**Effects of Ly$\alpha$ forest (IGM attenuation):** In addition to the emission lines variability, we show in Figures 12 and 13 the wavelength-dependent effects by IGM attenuation. At a wavelength range shorter than 1216Å , observed flux is attenuated due to intervening absorption systems (e.g., Madau 1995). To describe the IGM attenuation at these wavelengths, we convolve a power-law continuum with the Meiksin (2006) optical depth, which is

$$f_\lambda^{\rm dif}({\rm Ly}\alpha\ {\rm forest}) = e^{-\tau_{\rm eff}(z,\lambda)}f_\lambda^{\rm dif}({\rm continuum}) \quad ({\rm A5})$$

where (redshift and wavelength dependent) $\tau_{\rm eff}(z,\lambda)$ is defined as the sum of the optical depth of resonant scattering by Lyman transitions and photoelectric absorption. The transmissivity function is shown in Figure 16.

## B: REGRESSION INTERCEPTS AS A FUNCTION OF REDSHIFT

We here consider a flux−flux plot for a quasar light curve in which the regression line has positive intercept (as the case of Figure 3). $a(s,l) > 0$ indicates the ratio of flux $f_\nu(l)/f_\nu(s)$, which is the slope of a straight line that passes through the origin and the observed data points at some epoch, becomes smaller when the quasar becomes brighter. In this case, the photometric color $m_s - m_l$, defined as $+2.5\log(f_\nu(l)/f_\nu(s))$, becomes bluer-when-brighter. Similarly, if the regression intercept is negative, the color of the quasar becomes redder-when-brighter (Lyutyi & Doroshenko 1993; Hagen-Thorn 1997; Sakata et al. 2010, 2011). Note that, as discussed in Section 1, the color variability trend referenced here is that of the "observed" photometric color, which does not directly mean the spectral hardening (softening) of the AGN intrinsic continuum emission.

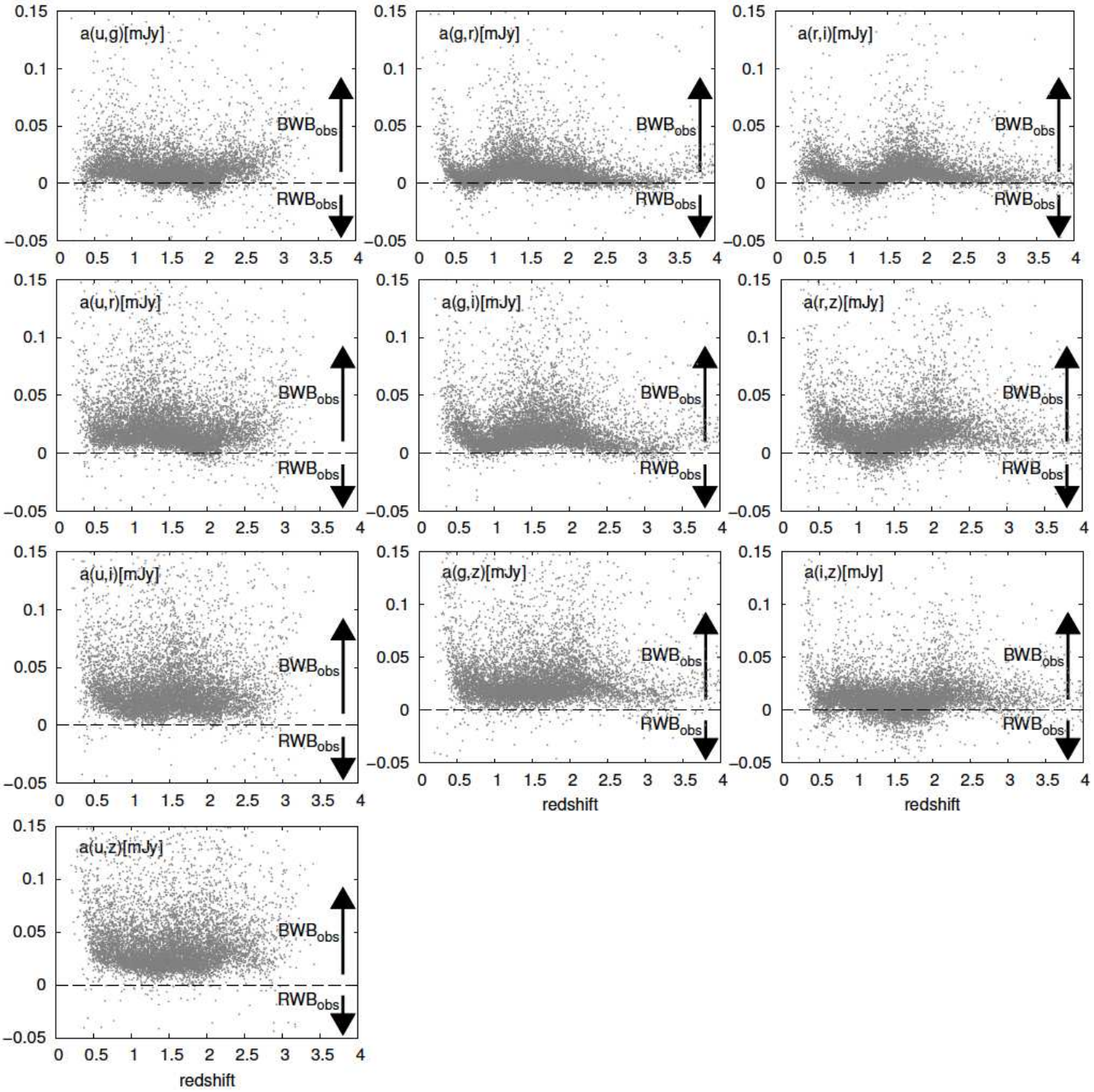


FIG. 17.— Regression intercepts as a function of redshift (dots). If $a(s,l) > 0$, the "observed" color tends to become bluer when the quasar becomes brighter($BWB_{obs}$ in Equation (B1)). And if $a(s,l) < 0$, the quasar has $RWB_{obs}$ trend.

Thus, the sign of the regression intercept in flux–flux space can be interpreted as the indicator of the "observed" photometric color variability. We express this fact as

$$\begin{cases} \mathrm{BWB_{obs}} & (\text{if } a(s,l) > 0) \\ \mathrm{RWB_{obs}} & (\text{if } a(s,l) < 0) \end{cases} \tag{B1}$$

where $BWB_{obs}$ and $RWB_{obs}$ indicates that the "observed" color becomes bluer when brighter and redder when brighter, respectively. Figure 17 shows the regression intercepts as a function of redshift for each quasar. Regression intercepts are generally positive, which indicates that the quasar color variability generally has $BWB_{obs}$ trend. Note that this result is merely another expression of the result shown in Figure 8, as the relation of $b^{\mathrm{ratio}}(s,l)$ and $b(s,l)$ (Equation (14)) is actually determined by the sign of $a(s,l)$.

REFERENCES


Abazajian, K., Adelman-McCarthy, J. K., Agüeros, M. A., et al. 2004, AJ, 128, 502, ADS
Abazajian, K. N., Adelman-McCarthy, J. K., Agüeros, M. A., et al. 2009, ApJS, 182, 543, ADS
Baldwin, J. A., Ferland, G. J., Korista, K. T., Hamann, F., & LaCluyzé, A. 2004, ApJ, 615, 610, ADS
Barth, A. J., Pancoast, A., Bennert, V. N., et al. 2013, ApJ, 769, 128, ADS
Bian, W.-H., Zhang, L., Green, R., & Hu, C. 2012, ApJ, 759, 88, ADS
Breedt, E., Arévalo, P., McHardy, I. M., et al. 2009, MNRAS, 394, 427, ADS
Cackett, E. M., Horne, K., & Winkler, H. 2007, MNRAS, 380, 669, ADS
Cagnoni, I., Fruscione, A., McHardy, I. M., & Papadakis, I. E. 1999, Mem. Soc. Astron. Italiana, 70, 29, ADS
Cameron, D. T., McHardy, I., Dwelly, T., et al. 2012, MNRAS, 422, 902, ADS
Cappellari, M., Scott, N., Alatalo, K., et al. 2013, MNRAS, 432, 1709, ADS
Chelouche, D. 2013, ApJ, 772, 9, ADS
Choloniewski, J. 1981, Acta Astron., 31, 293, ADS
Collier, S., Horne, K., Wanders, I., & Peterson, B. M. 1999, MNRAS, 302, L24, ADS
Croom, S. M., Richards, G. T., Shanks, T., et al. 2009, MNRAS, 392, 19, ADS
Davis, S. W., Woo, J.-H., & Blaes, O. M. 2007, ApJ, 668, 682, ADS
Dexter, J., & Agol, E. 2011, ApJ, 727, L24, ADS
Dietrich, M., Hamann, F., Appenzeller, I., & Vestergaard, M. 2003, ApJ, 596, 817, ADS
Doi, M., Tanaka, M., Fukugita, M., et al. 2010, AJ, 139, 1628, ADS
Dong, X.-B., Wang, J.-G., Ho, L. C., et al. 2011, ApJ, 736, 86, ADS
Feigelson, E. D., & Jogesh Babu, G. 2012, Modern Statistical Methods for Astronomy, ADS
Ferland, G. J., Hu, C., Wang, J.-M., et al. 2009, ApJ, 707, L82, ADS
Gil-Merino, R., Goicoechea, L. J., Shalyapin, V. N., & Braga, V. F. 2012, ApJ, 744, 47, ADS
Giveon, U., Maoz, D., Kaspi, S., Netzer, H., & Smith, P. S. 1999, MNRAS, 306, 637, ADS
Glass, I. S. 2004, MNRAS, 350, 1049, ADS
Glikman, E., Helfand, D. J., & White, R. L. 2006, ApJ, 640, 579, ADS
Goad, M. R., Koratkar, A. P., Axon, D. J., Korista, K. T., & O'Brien, P. T. 1999a, ApJ, 512, L95, ADS
Goad, M. R., Koratkar, A. P., Kim-Quijano, J., et al. 1999b, ApJ, 524, 707, ADS
Goad, M. R., Korista, K. T., & Ruff, A. J. 2012, MNRAS, 426, 3086, ADS
Goad, M. R., O'Brien, P. T., & Gondhalekar, P. M. 1993, MNRAS, 263, 149, ADS
Grandi, S. A. 1982, ApJ, 255, 25, ADS
Gu, M. F., & Li, S.-L. 2013, A&A, 554, A51, ADS
Guo, H., & Gu, M. 2013, ArXiv e-prints, arXiv:1306.0273, ADS
Hagen-Thorn, V. A. 1997, Astronomy Letters, 23, 19, ADS
Halpern, J. P., Leighly, K. M., & Marshall, H. L. 2003, ApJ, 585, 665, ADS
Hawkins, M. R. S. 1993, Nature, 366, 242, ADS
—. 2003, MNRAS, 344, 492, ADS
Hewett, P. C., & Wild, V. 2010, MNRAS, 405, 2302, ADS
Hopkins, P. F., Strauss, M. A., Hall, P. B., et al. 2004, AJ, 128, 1112, ADS
Hryniewicz, K., Czerny, B., Pych, W., et al. 2013, ArXiv e-prints, arXiv:1308.3980, ADS
Hu, C., Wang, J.-M., Ho, L. C., et al. 2008, ApJ, 687, 78, ADS
Hubeny, I., Agol, E., Blaes, O., & Krolik, J. H. 2000, ApJ, 533, 710, ADS
Kato, S., Fukue, J., & Mineshige, S. 2008, Black-Hole Accretion Disks — Towards a New Paradigm —, ADS
Kawaguchi, T., Mineshige, S., Umemura, M., & Turner, E. L. 1998, ApJ, 504, 671, ADS
Kawaguchi, T., Shimura, T., & Mineshige, S. 2001, ApJ, 546, 966, ADS
Kishimoto, M., Antonucci, R., Blaes, O., et al. 2008, Nature, 454, 492, ADS
Korista, K. T., & Goad, M. R. 2001, ApJ, 553, 695, ADS
—. 2004, ApJ, 606, 749, ADS
Kouzuma, S., & Yamaoka, H. 2012, ApJ, 747, 14, ADS
Krawczyk, C. M., Richards, G. T., Mehta, S. S., et al. 2013, ApJS, 206, 4, ADS
Krolik, J. H., Horne, K., Kallman, T. R., et al. 1991, ApJ, 371, 541, ADS
Krolik, J. H., & Kallman, T. R. 1988, ApJ, 324, 714, ADS
Kurk, J. D., Walter, F., Fan, X., et al. 2007, ApJ, 669, 32, ADS
Landt, H., Elvis, M., Ward, M. J., et al. 2011, MNRAS, 414, 218, ADS
Li, S.-L., & Cao, X. 2008, MNRAS, 387, L41, ADS
Lira, P., Arévalo, P., Uttley, P., McHardy, I., & Breedt, E. 2011, MNRAS, 415, 1290, ADS
Lynden-Bell, D. 1969, Nature, 223, 690, ADS
Lyutyi, V. M., & Doroshenko, V. T. 1993, Astronomy Letters, 19, 405, ADS
MacLeod, C. L., Ivezić, Ž., Sesar, B., et al. 2012, ApJ, 753, 106, ADS
Madau, P. 1995, ApJ, 441, 18, ADS
Maoz, D., Markowitz, A., Edelson, R., & Nandra, K. 2002, AJ, 124, 1988, ADS
Maoz, D., Netzer, H., Peterson, B. M., et al. 1993, ApJ, 404, 576, ADS
Markwardt, C. B. 2009, in Astronomical Society of the Pacific Conference Series, Vol. 411, Astronomical Data Analysis Software and Systems XVIII, ed. D. A. Bohlender, D. Durand, & P. Dowler, 251, ADS
Marshall, H. L., Carone, T. E., Peterson, B. M., et al. 1997, ApJ, 479, 222, ADS
Marshall, K., Ryle, W. T., & Miller, H. R. 2008, ApJ, 677, 880, ADS
Meiksin, A. 2006, MNRAS, 365, 807, ADS
Meusinger, H., Hinze, A., & de Hoon, A. 2011, A&A, 525, A37, ADS
Meusinger, H., & Weiss, V. 2013, A&A, 560, A104, ADS
Novak, G. S., Faber, S. M., & Dekel, A. 2006, ApJ, 637, 96, ADS
Paltani, S., & Courvoisier, T. J.-L. 1994, A&A, 291, 74, ADS
Paltani, S., & Walter, R. 1996, A&A, 312, 55, ADS
Park, D., Kelly, B. C., Woo, J.-H., & Treu, T. 2012, ApJS, 203, 6, ADS
Pereyra, N. A., Vanden Berk, D. E., Turnshek, D. A., et al. 2006, ApJ, 642, 87, ADS
Phillips, K. C., & Meszaros, P. 1986, ApJ, 310, 284, ADS
Richards, G. T., Fan, X., Schneider, D. P., et al. 2001, AJ, 121, 2308, ADS
Richards, G. T., Hall, P. B., Vanden Berk, D. E., et al. 2003, AJ, 126, 1131, ADS
Sakata, Y., Morokuma, T., Minezaki, T., et al. 2011, ApJ, 731, 50, ADS
Sakata, Y., Minezaki, T., Yoshii, Y., et al. 2010, ApJ, 711, 461, ADS
Schlegel, D. J., Finkbeiner, D. P., & Davis, M. 1998, ApJ, 500, 525, ADS
Schmidt, K. B., Rix, H.-W., Shields, J. C., et al. 2012, ApJ, 744, 147, ADS
Shakura, N. I., & Sunyaev, R. A. 1973, A&A, 24, 337, ADS
Shang, Z., Brotherton, M. S., Green, R. F., et al. 2005, ApJ, 619, 41, ADS
Shemmer, O., Uttley, P., Netzer, H., & McHardy, I. M. 2003, MNRAS, 343, 1341, ADS
Shen, Y., Richards, G. T., Strauss, M. A., et al. 2011, ApJS, 194, 45, ADS
Shields, J. C. 2007, in Astronomical Society of the Pacific Conference Series, Vol. 373, The Central Engine of Active Galactic Nuclei, ed. L. C. Ho & J.-W. Wang, 355, ADS
Suganuma, M., Yoshii, Y., Kobayashi, Y., et al. 2006, ApJ, 639, 46, ADS
Terlevich, R., Tenorio-Tagle, G., Franco, J., & Melnick, J. 1992, MNRAS, 255, 713, ADS
Tomita, H., Yoshii, Y., Kobayashi, Y., et al. 2006, ApJ, 652, L13, ADS
Torricelli-Ciamponi, G., Foellmi, C., Courvoisier, T. J.-L., & Paltani, S. 2000, A&A, 358, 57, ADS
Tremaine, S., Gebhardt, K., Bender, R., et al. 2002, ApJ, 574, 740, ADS
Trèvese, D., & Vagnetti, F. 2002, ApJ, 564, 624, ADS
Tsuzuki, Y., Kawara, K., Yoshii, Y., et al. 2006, ApJ, 650, 57, ADS
Vanden Berk, D. E., Richards, G. T., Bauer, A., et al. 2001, AJ, 122, 549, ADS
Vanden Berk, D. E., Wilhite, B. C., Kron, R. G., et al. 2004, ApJ, 601, 692, ADS
Vanden Berk, D. E., Shen, J., Yip, C.-W., et al. 2006, AJ, 131, 84, ADS
Vestergaard, M., & Wilkes, B. J. 2001, ApJS, 134, 1, ADS
Walsh, J. L., Minezaki, T., Bentz, M. C., et al. 2009, ApJS, 185, 156, ADS
Wamsteker, W., Rodriguez-Pascual, P., Wills, B. J., et al. 1990, ApJ, 354, 446, ADS
Webb, W., & Malkan, M. 2000, ApJ, 540, 652, ADS
Wilhite, B. C., Vanden Berk, D. E., Kron, R. G., et al. 2005, ApJ, 633, 638, ADS
Williams, M. J., Bureau, M., & Cappellari, M. 2010, MNRAS, 409, 1330, ADS
Wills, B. J., Netzer, H., & Wills, D. 1985, ApJ, 288, 94, ADS
Winkler, H. 1997, MNRAS, 292, 273, ADS
Winkler, H., Glass, I. S., van Wyk, F., et al. 1992, MNRAS, 257, 659, ADS
Woo, J.-H. 2008, AJ, 135, 1849, ADS
Woo, J.-H., Treu, T., Malkan, M. A., Ferry, M. A., & Misch, T. 2007, ApJ, 661, 60, ADS
Yip, C. W., Connolly, A. J., Vanden Berk, D. E., et al. 2004, AJ, 128, 2603, ADS
Zhang, X.-G. 2013, MNRAS, 435, 2141, ADS
Zuo, W., Wu, X.-B., Liu, Y.-Q., & Jiao, C.-L. 2012, ApJ, 758, 104, ADS